Analytical Tweezers for cell manipulation and diagnostic

Inês A. Carvalho
Mestrado em Física Médica
Departamento de Física e Astronomia
2021

Orientador
Prof. Dr. Pedro A. S. Jorge, Faculdade de Ciências da Universidade do Porto e INESC TEC

Coorientador
Prof. Dr. Carla Carmelo Rosa, Faculdade de Ciências da Universidade do Porto e INESC TEC

U.PORTO

FACULDADE DE CIÊNCIAS
UNIVERSIDADE DO PORTO

Todas as correções determinadas pelo júri, e só essas, foram efetuadas.

O Presidente do Júri,

Porto, _____/_____/_____

UNIVERSIDADE DO PORTO

MASTERS THESIS

Analytical Tweezers for cell manipulation and diagnostic

Author:
Inês CARVALHO

Supervisor:
Pedro JORGE

Co-supervisor:
Carla Carmelo ROSA

A thesis submitted in fulfilment of the requirements for the degree of MSc. Medical Physics

at the

Faculdade de Ciências da Universidade do Porto
Departamento de Física e Astronomia

November 30, 2021

" There are probably few people who do not dream of the good old times, when doing science often meant fascination, excitement, even adventure. In our time, doing science involves often technology and, perhaps, even business. But there are still niches where curiosity and fascination have their place (...) "

written by Prof. Dr. Karl Otto Greulich

Acknowledgements

The past year has been marked by the challenges posed by this dissertation. I am sincerely grateful to all the wonderful people who, during this time, believed in my capabilities and kept me motivated:

First of all, to my supervisor, Dr Pedro Jorge, for walking me through the first steps, challenging me to explore new problems and distinct areas. For always hearing my point of view and allowing me to make my own choices, trusting in my potential. More importantly, thank you for keeping me on track and never letting me give up on my goals.

I would also like to thank my cosupervisor, Dr Carla Rosa. For her help, for her patience and extraordinary point of view. Thank you for all the time helping and teaching me on how to better overcome the experimental problems and, for always motivating me throughout the dissertation.

To Dr. Nuno Silva, a special thank you for the help throughout the last part of the dissertation and for supporting me when I needed the most. For teaching me to be more patient and to better deal with daily problems. Thank you for the effort, dedication, kindness and tireless work.

To Dr. Luís Coelho and to Dr. Paulo Marques thank you for all the time you took to help me find a solution to the experimental obstacles. Thanks for your patience and kindness.

To Dr. Teresa Borges, a especial thanks for the microalgae samples, indispensable to the dissertation project.

To all my colleagues from the Center of Applied Photonics at INESC-TEC, especially to João Mendes, Catarina Monteiro, António Rodrigues and Bernardo Azevedo, thanks for helping me and for the patience through my difficulties. To Sandra Rodrigues and Filipe Marques, thank you for guiding me through the first part of my dissertation.

To the best colleagues, a special thanks to Laura Providência, Sara Freitas and João Marques, for always believing in me. Thanks for the long conversations, for the love and support during this dissertation. Thanks for encouraging me to work harder through the most difficult times.

To Alexandra Fernandes, Fabrizio Dodat and Fernando Bior, a special thanks for being unique friends and always supporting me to work more. I am very grateful for your friendship.

To my parents and sister, thank you for always supporting and loving me regardless my unique personality. Thanks for the values and advices over the years, and for always believing in my capabilities. I am very proud to be your family.

To José Bastos, my boyfriend, thanks for the love, support and patience during all these years, especially in the last months.

To my family and most closed friends, thanks for the constant faith and support. To my cousin Diogo Figueira and aunt Florinda Conceição, thanks for providing me lovely times and for always being there for me.

UNIVERSIDADE DO PORTO

Abstract

Faculdade de Ciências da Universidade do Porto
Departamento de Física e Astronomia

MSc. Medical Physics

Analytical Tweezers for cell manipulation and diagnostic

by Inês CARVALHO

Over the last years, the search for reliable biosensing devices is growing, focusing on more efficient treatments and more timely prevention of diseases. Optical tweezers, as one of the emergent tools for modern biotechnology, has proven the ability to trap and manipulate individual particles and cells, in a non invasive way. In fact, the unique features of optical tweezers have been used to explored the classification of individual specimens, from different approaches, for instance, the back scattered radiation has been explored for applications in the biomedical field. In this dissertation, we explore the assembly of a conventional optical tweezers system with the ability to manipulate micron-sized particles and cells. In particular, we explore the analysis of the forward scattered radiation, collected using a position sensitive quadrant photodetector. We introduce a novel pre-processing procedure for the extraction of relevant features for class classification.

In the first place, an overview of the state of the art of conventional optical tweezers is described, where we explore the use of alternative configurations for desirable optical trapping fields. Also, we discuss various purposes for the classification of specimens, presented in the literature. In the following chapter, we present the principles of optical tweezers discussing three-dimensional optical trapping and its limitations. Additionally, we discuss the dynamics of the trapped Brownian particle and some of the methods useful to characterize the particle dynamics and the strength of the trap system. After that, the characterization of the conventional optical tweezers is addressed, presenting the tools and techniques used throughout this dissertation, along with the experimental results obtained.

In the last part of the dissertation, we present a methodology based on a pre-processing strategy that combines Fourier transform and principal component analysis to reduce the

dimension of the data and perform relevant feature extraction. We test several standard machine learning algorithms, for distinction of particles and cells. The low computational footprint methods employed proved the ability to achieve accuracy performances around 90%. We were able to discriminate between distinct micron-sized particles, to classify different cells and even discriminate nanoparticles.

In summary, in this dissertation, we proved the capacity of classification of trapped specimens with a conventional optical tweezers system, based on a novel processing strategy. Also, we were able to demonstrate the benefits of using a quadrant photodetector against a standard detector to probe the forward scattered radiation, for particle classification from the signals it provides.

UNIVERSIDADE DO PORTO

Resumo

Faculdade de Ciências da Universidade do Porto
Departamento de Física e Astronomia

Mestrado em Física Médica

Pinças óticas analíticas para a manipulação e diagnóstico de células

por Inês CARVALHO

Ao longo dos últimos anos, a procura por biossensores mais confiáveis tem crescido, com foco em tratamentos mais eficientes e numa prevenção mais atempada de doenças. As pinças óticas, como uma das ferramentas emergentes para a biotecnologia moderna, têm provado a capacidade de aprisionar e manipular partículas e células individuais, de uma forma não invasiva. De facto, as características únicas das pinças óticas têm sido utilizadas para explorar a classificação de espécimes individuais, a partir de diferentes abordagens, tal como a radiação de retroespalhamento, que tem sido explorada para aplicação na biomedicina. Nesta dissertação, exploramos um sistema convencional de pinças óticas com a capacidade de manipular partículas micrométricas e células. Em particular, exploramos a análise da radiação de espalhamento frontal, coletada com um detetor de quadrantes sensível à posição. Foi também introduzido um procedimento de pré processamento para a extração de características relevantes para a classificação de classe.

Em primeiro lugar, foi descrita uma revisão do estado da arte das pinças óticas convencionais, onde a utilização de configurações alternativas para a obtenção de campos óticos de aprisionamento desejados foi explorada. Em adição, foram discutidas as várias abordagens para a classificação de espécimes, que estão presentes na literatura. No capítulo seguinte, apresentamos os princípios das pinças óticas onde o aprisionamento ótico em três dimensões foi abordado, assim como as suas limitações. Além disso, a dinâmica das partículas aprisionadas e alguns dos métodos úteis para a caracterização das partículas e da força do sistema de aprisionamento, foram discutidos. De seguida, a caracterização do sistema convencional de pinças óticas foi apresentada, onde as ferramentas e as técnicas utilizadas ao longo desta dissertação foram abordadas, assim como os resultados experimentais obtidos.

Na última parte da dissertação, apresentamos uma metodologia baseada numa estratégia de pré-processamento que combina a transformada de Fourier com a análise de componentes principais para a redução da dimensão dos dados de forma a extrair características relevantes. Testámos diversos algoritmos padrão de *machine learning* para a distinção de partículas e células. A reduzida pegada computacional dos métodos utilizados provou a capacidade de obter precisões da ordem dos 90%. Conseguimos discriminar entre distintos tipos de partículas micrométricas, de classificar diferentes células e ainda discriminar nanopartículas.

Em resumo, nesta dissertação, provamos a capacidade de classificação de espécimes aprisionadas com um sistema de pinças óticas convencionais, baseado numa nova estratégia de processamento. Além disso, demonstramos os benefícios da utilização de um detetor de quadrantes em relação a um detetor padrão, para a classificação de partículas através do sinal de espalhamento frontal.

Contents

List of Figures

Glossary

3D	3 Dimensions
BFP	Back Focal Plane
CAP	Center of Applied Photonics
CMOS	Complementary Metal-Oxide-Semiconductor
COT	Conventional Optical Tweezers
DAQ	Data Acquisition Board
DNA	deoxyribonucleic acid
EP	Equipartition
EVs	Extracellular Vesicles
FFT	Fast Fourier Transform
FOT	Fiber Optical Tweezers
FWHM	Full Width at Half Maximum
INESC TEC	INESC Technology and Science
IR	Infrared
KNN	K-Nearest Neighbors
KPA	K-Cube Beam Position Aligner
KPZ	K-Cube Piezo Controller
LED	Light Emitting Diode
NA	Numerical Aperture
NIR	Near-Infrared
NN	Neural Networks

OT	Optical Tweezers
PCA	Principal Component Analysis
PMMA	Polymethyl Methacrylate
POT	Plasmonic Optical Tweezers
PS	Polystyrene
PSD	Power Spectral Density
PZT	Piezoelectric
QPD	Quadrant Photodetector
RF	Random Forests
SIBA	Self-Induced Back-Action
SVM	Support Vector Machines
TEC	Thermoelectric cooler
TSG	T-Cube Strain Gauge Reader

Chapter 1

Introduction

1.1 Context

In 1619, Keppler proposed that the deflection of comet tails entering our Solar System could be due to the mechanical effect of light. Some years later, Maxwell jointly with the four equations that describe all theories of electromagnetism predicted that the radiation field carries momentum, and that light should in fact be able to exert pressure and forces on matter. But it was only after the 1960s, following the discovery of the laser, that the journey of optical tweezers started [1].

The curiosity and perseverance of Arthur Ashkin and his coworkers allowed the discovery of optical tweezers in the decade of 70's. Ashkin demonstrated that light, due to its intrinsic property, momentum, could be used to trap and suspend particles, without causing damage. The momentum transfer from the light to the particle, together with the balance of the resulting forces, allows for the phenomenon of optical trapping to occur [2]. For all the contributions that Arthur Ashkin brought to the world of science and technology, he was recently awarded the 2018 Nobel prize in Physics [3].

Nowadays, optical tweezers are used on fundamental studies in the area of life sciences, in particular for studying the mechanical properties and sorting of living cells [4, 5]. The fast developments in the optical tweezers system and the advanced algorithms, allowed to usher in new studies of physical and chemical properties of living tissues, as well as of unknown biomechanics in biological processes [5]. More recently, the light scattered from the trapped particles has been considered for analysis as it may carry information related to the particle properties, such as diameter, refractive index, composition, or others, which could enable early diagnosis tools, an asset in the field of healthcare [6].

1.2 Optical tweezers in biological sciences

In his first experiment in the early 1970's, Ashkin reported the effect of optical trapping of micron-sized particles with two counterpropagating laser beams. The observation of particles trapped and accelerated in the interference region was the first demonstration of radiation pressure at microscale [7]. Only after 16 more years, Ashkin and his coworkers realized that light could trap particles using solely a single tightly focused beam, introducing the concept of Optical Tweezers [2]. Since then, the study and manipulation of micron and submicron dielectric particles and individual atoms became possible [8, 9].

Optical tweezers explore optically-induced forces generated by a tightly focused beam. The trapping results from the balance of the gradient force with the scattering force, which creates an effective three-dimensional (3D) potential. The first component is related to the spatial distribution of the optical intensity, and the latter is associated with the radiation pressure and photon momentum transfer. This process allows 3D manipulation, considering the target specimen fulfils certain criteria regarding its refractive index and size [4, 10].

Concerning biological specimens, the first applications of single-beam gradient traps were reported in 1987, with the optical trapping and manipulation of individual viruses, bacteria [11], and live single cells [12]. Later on, Berns et al. reported the first manipulation of cell organelles and chromosomes. It was established that the optical forces could be used to further study the chromosomes movement during cell division [13]. Given the unique non-invasive characteristic of optical tweezers, which avoids complications related to contamination and thermal damage, they became, beyond doubt, extensively used over the decades, for different purposes.

These days, optical tweezers are a well-established tool in biological research to probe physical properties and manipulate biological specimens. In particular, the ability to manipulate and exert forces has been explored in multiple contexts from dragging bacteria, microalgae and blood cells *in vivo* [14], to stretching and bending single macromolecules, such as DNA and RNA [15], just to name a few. Concerning the study and the characterization of the specimen, applications of optical tweezers spans across probing forces exerted by molecular motors [4, 16], classifying cancer cells [17] and chromosome sorting [4, 16].

One field of application of optical tweezers in biological sciences is the study and diagnosis of diseases. For example, measuring the elastic properties of blood cells can be

used to identify pathological conditions, such as malaria and diabetic retinopathy [18]. Also, analysing the dynamics of nanoscale structures in optical tweezers, such as extracellular vesicles (EVs), lipoproteins, and virus, may provide information regarding the human physiology or even clinical conditions [19]. Indeed, being related with the mechanisms of cancer and neurodegenerative diseases [20], sorting and analyzing EVs is a way to obtain an early diagnosis and prognosis of such diseases [20].

Another subject where optical tweezers are extensively used is in the field of neuroscience, which appeared more recently, in part due to the brain complexity [21]. For instance, Prada et al. recently reported the trapping and manipulation of EVs produced by glial cells. By moving the extracellular vesicles onto neurons, the effect of a specific protein was studied. It was reported that a prolonged exposure to inflammatory EVs can lead to reduction in the dentritic spine density and consequently a decrease in strength of excitatory synapses [22]. For neuroscience, the dynamics of the environment where neurons are may influence their behaviour, and so, it is desirable to perform *in vivo* measurements.

So far we focused briefly on applications and presented a non-exhaustive review of the most important results. In the next sections, we focus the discussion on the experimental setups and methods of the optical tweezers systems, focusing on the calibration of the system and the analysis of the trapping specimen through signal processing. To finalize, we discuss some alternative setups and methodologies that aim to address challenges, such as the miniaturization of setups beyond the diffraction limit.

1.3 Optical tweezers systems

A conventional optical tweezers system, as the one used in this dissertation, is based on an inverted microscope configuration. In short, the trapping laser is tightly focused with a microscope objective into a sample. The control can be performed with an imaging system that images the sample. The detection can be performed by a photodetector that collects the forward scattered radiation of a trapped particle. The functionalization of the system requires calibration procedures, such as position, force and stiffness determination.

The first calibrations were attempted by video-based position detection systems, which suffer from low spatial and temporal resolutions [23]. Video-based methods are still employed for position detection, even tough they are limited in the detection bandwidth,

which depends on the image acquisition speed, and the respective camera frame rates. On the other hand, laser-based position detection systems, such as a quadrant photodetector (QPD), present better spatial and temporal resolution for calibration purposes [4].

1.3.1 Laser-based position detection scheme

For accurate particle displacement detection, the laser-based system explores the changes that the forward laser beam undergoes upon interaction with the trapped particle, and its relation with the intrinsic induced change in the momentum of a trapped bead. One of the most popular schemes employed for laser-based position detection in conventional optical tweezers systems is the back focal plane (BFP) detection [4].

BFP detection is based on the interference between the forward-scattered light and the remaining light, as seen in Figure 1.1 [24]. The lens images the back focal plane of the back aperture of the condenser lens onto the quadrant photodetector, allowing to probe for lateral movement as reported by Gittes and Schmidt. Additionally, Rohrbach and Stelzer reported that three-dimensional position detection of a trapped particle could also be achieved by relating the axial position variation with the detected signal [25]. Indeed, while lateral displacements generate asymmetry in the pattern itself, the axial movement introduces changes to the total intensity on the detector [26], allowing to effectively probe the dynamics in 3D [25].

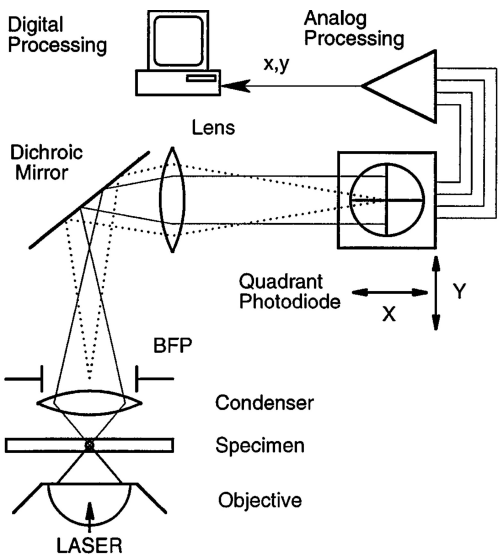

FIGURE 1.1: Experimental setup for laser-based position detection- BFP detection [24].

As mentioned above, a common method to characterize the optical tweezers system, is through the calculation of the optical forces, for which a proper calibration of the trap

is required [4]. Allersma et al. reported the analysis of position fluctuations as an indirect way to determine the detector sensitivity. Additionally, the position response of the detector, i.e., the conversion factor related to the measured units in the detector and the real displacement of the trapped particles, can be estimated [27]. With these in mind, considering a back focal plane detection scheme, the displacement of a bead through the focus region can be accomplished either with a controlled movement of a bead fixed to the surface along the detector region, or by means of a steerable trap [4]. Precise position calibration is essential, to probe dynamics and compute optical forces.

1.3.2 Optical forces characterization

One of the first ways to measure the optical force was to trap a particle at a high power and slowly reducing it to the point where the particle escaped. Ashkin et al. adapted this approach, taking advantage of the trapping system itself, and used a video capture for force measurements, from what the calibration was accomplished [28]. Over time, quantitative measurements of forces acting in cellular systems have been reported with optical tweezers [14] and rely on accurate characterization of the trap [29].

The characterization of the trap can be achieved mainly by three approaches - the active, the passive and the direct calibration methods. In most cases, in particular for the case of Gaussian modes, the force applied by the optical trap can be modeled as an harmonic spring [29], and the system characterized by a stiffness constant.

Considering the active stiffness calibration method, the trap stiffness is obtained through the calibration of the optical force exerted by the laser beam, while a movement is initiated by an external force [29]. One example, is the drag force method where the displacement of the trapped particle is measured relatively to the center of the trap, being highly dependent on the viscous forces produced by the medium. In this case, the bead is displaced by an external force and the speed at which the particle is trapped is measured [4]. Moreover, when the particle is too close to the surface, the viscous drag coefficient must be corrected [15].

The passive stiffness calibration methods are related to the thermal fluctuations of the trapped particle. The equipartition method, the power spectral density method and the Boltzmann statistics are examples of such calibration methods [29], that will be extensively described in section 2.3. Considering the equipartition method, the trap stiffness is determined by measuring the position variance of the trapped particle [4]. Differently,

the power spectral density method determines the trap stiffness by fitting a Lorentzian function to the power spectrum of the Brownian motion of a bead in the optical trap [30]. In Boltzmann statistics, the complete distribution of the thermal position fluctuations of the trapped particle is considered to determine the trap stiffness [31].

Finally, in direct stiffness calibration methods, the measurements of the forces are based on the conservation of linear momentum [32]. This method can be employed in dual optical trapping setups, and requires modeling the force with ray optics theory and relating with the scattered light exiting from the trap [33].

We presented a few calibration procedures focusing on those employed in this dissertation. A complete overview of other existing methods can be found in reference [34].

1.4 Signal analysis of optically trapped particles and cells

In optical trapping experiments, trapped specimens, such as particles and cells, express themselves in different ways through the analysis of the scattered signal. For instance, biophysical changes can be observed in cells and linked to the differentiation between healthy and non healthy cells [35]. This way, the scattering signal from optical tweezers assays can be processed by advanced signal processing methodologies to achieve specimens differentiation and classification.

1.4.1 Classification of trapped particles and cells

ptical tweezers are a valuable tool for sorting, identifying and even manipulating single specimens [36, 37]. For this purpose, the role of signal processing and analysis is of critical importance, taking advantage from recent advances of artificial intelligence algorithms to improve the interpretation of more complex data and the classification of novel particles [38]. Random Forests and Neural Networks are representative of some of the algorithms that recognize patterns and are able to classify novel samples [19]. The classification task has been reported for various purposes and it can be divided into three main approaches.

The first approach uses spatial image information, which can be obtained from the microscope lens that allows imaging of the sample [39, 40], or even the analysis of the spatial scattering pattern and the subsequent analysis of the fringes and speckles [41]. In

both cases, the classification task can benefit from machine-learning approaches, however it is limited to the spatial and temporal resolution of the optical imaging system.

Another common methodology for the classification task is based on the combination of optical tweezers with Raman spectroscopy, in order to perform single particle analysis [42]. With this technique, the identification of a cell as being cancerous or healthy has been successfully reported based on the spectral signature of the trapped cells obtained [43]. When combining this with a multitude of machine-learning algorithms, the extraction of the relevant features derived from the spectrum can be performed and consequently used to train the algorithms [44]. Despite being appealing, the cost of the system is highly increased due to the addition of the spectrometer. Furthermore, it usually depends on relatively long integration times, decreasing the ability for a high throughput.

The third approach is related to the analysis of the signal scattered from trapped particles/cells in the temporal domain, for the classification purpose, as the scattering signal has information related to particle-specific characteristics and behavior. In practice, as the scattered signal is directly related to the physical dynamics of the trapped particles/cells, it has been used for many proposes, such as, to explore Brownian motion [45, 46] and for optical force calculation [47]. In fact, Lenton et al. explored the optical forces acting on a spherical particle with a neural network algorithm, and the analysis of the behaviour of optically trapped particles in complex light fields has also been reported [47].

Still related to the third approach, the scattering signal temporal dynamics has been explored with optical fiber tweezers [48, 49]. Paiva et al. reported an experiment where a polymeric lensed optical fiber was developed for simultaneously trapping and collecting the back scattered signal [19]. Later, after processing the data, the same author reported the discrimination of two gastric cancer cell models. For that purpose, features were extracted from the temporal and Fourier domain, which allowed to train a standard random forest algorithm [17]. Taking into consideration that the only difference between the cancer models was their corresponding surface glycosylation, this approach showed great potential for biomedical applications [6, 17]. Therefore, the possibility of classification of trapped particles and cells can have a strong impact in the early diagnosis and prognosis of diseases.

1.4.2 Forward scattered light analysis

On a conventional optical tweezers system, we can analyse the forward or back scattered signal from a trapped specimen. In this work we focus on the analysis of the forward scattered signal.

As a matter of fact, much information can be retrieved from the forward scattered signal. For example, Pang and Gordon observed that the trapping of nanoparticles with a double-nanohole in a gold film produces changes in the optical transmission that varied with the optical force produced [50]. A year later, they reported the trapping of a single protein molecule, and by using a shorter wavelength, observed better detection efficiency and capability to unfold the protein. When the protein was trapped, a jump in the transmission signal was verified which is related to the motion of the particle inside the aperture, i.e. to the Brownian motion of the trapped molecule. The authors reported different states of trapping of the forward scattered signal and concluded that the double-step observed, see Figure 1.2, was generated due to the transitions between the normal form and elongated form of the molecule, which features larger polarizability and thus provides a stronger trapping potential [51, 52].

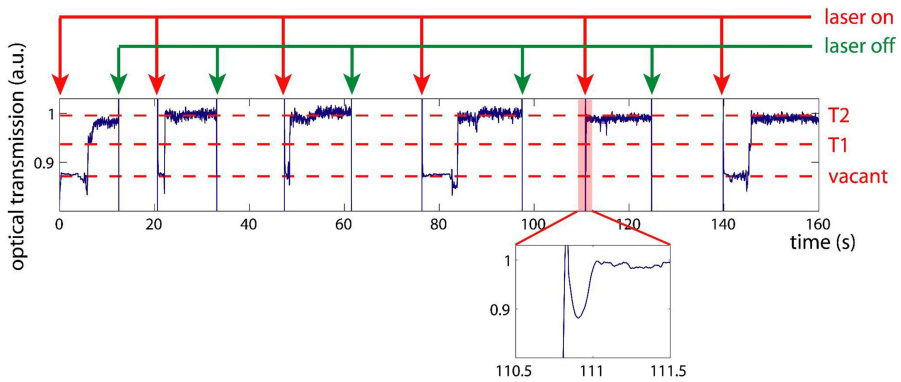

FIGURE 1.2: Time signal of the optical power transmitted through the double-nanohole. It is shown the optical transmission behaviour when the laser is turned on, when the laser is turned off and the different trapped states for the protein molecule [51].

1.5 Alternative optical tweezers configurations

While it can be used for most of the typical applications, conventional optical tweezers struggle to perform challenging tasks, such as trapping at the nanoscale or in vivo environments. Howbeit, one strategy could be to increase the trapping laser power, this could lead to thermal damage of the particles/cells. To solve this problem, new strategies

and systems have been explored to enable the manipulation of nanosized specimens, as well as the assessment of different depths in the media.

1.5.1 Fiber optical tweezers configurations

When the target particle is located deep within the medium, in particular, for the manipulation of cells in biological tissue, the focusing becomes more difficult and the conventional approach becomes limited [21]. In these situations, one solution is the use of simple optical trapping alternatives with a reduced footprint. Fiber Optical Tweezers (FOT) emerged as suitable candidates for trapping, while being simpler and less costly in comparison to conventional systems [6, 53].

The trapping with fiber optical tweezers can be employed with optical fibers whose extremity has been modified to form a lens, or has been changed to a particular pattern. This approach offers the advantage of being miniaturized and more flexible. However, the beam created for the trap is not as tightly focused as the one resulting from a microscope objective. Consequently, the gradient forces are often weaker, and the trapping in three dimensions is more difficult to accomplish [6, 21]. Nevertheless, the geometrical features of the fiber tip can be engineered to shape the trapping intensity patterns, and thus enhance or control the trapping effect [53].

Fiber optical tweezers can also be used in a counter-propagating configuration, ensuring a better axial stability. Moreover, to improve the trapping depth within scattering media, several approaches have been reported [21], such as tapered fibers, fibers with coated or etched tips [53, 54] and even with multi-mode fibers in holographic optical tweezers configurations [55].

1.5.2 Plasmonic optical tweezers configurations

Conventional optical tweezers can perform the trapping of micron-sized particles without major difficulties [56] and, at a much smaller scale, similar strategies can be used to trap atoms [9]. But in the range in between, the nanometre scale, several difficulties were found, as efficiency is lost due to the smaller diameter of the particles [57]. At this scale, it is no longer possible to perform the trapping with conventional optical tweezers systems due to the decrease of the optical force and to the diffraction limit, inherent to the system [58]. In this context, the subject of plasmonics has been extensively studied in the recent years.

Plasmonics is based on the collective oscillations (plasmons) of the free electron density present on a metal structure [58], which can be stimulated by incident light [59]. One of the most relevant features of plasmonics is the opportunity to generate highly localized evanescent fields, and the capability to confine light in scales below the optical wavelength. This way, high field gradients occur in the optical near-field [1, 59] and allow trapping in the nanometer regime.

One of the first configurations explored was a sharp metal tip illuminated by a laser, reported in 1997. This metal tip offered highly localized evanescent fields close to the surface of the tip, increasing the trapping force in a smaller region [60]. After that, Okamoto and Kawata reported the analysis of the force exerted on a sub wavelength dielectric sphere by an evanescent field. The light was transmitted through a sub wavelength nanoaperture in a metallic film, and the particle is located right above the aperture. They evaluated the spatial distribution of the light intensity as well as the force distribution, and found dependence on light polarization [61]. Later, Juan et al. proposed the trapping of a nanometre polystyrene sphere considering a nanoaperture in a metal film. This configuration revealed a different trapping mechanism [62], where the position of the trapped particle changes the resonance frequency of the resonator and affects the field that is acting on it, an effect known as the self-induced back-action [1, 63]. This effect is useful for enhancing the trapping force in a way that the manipulation, of virus and quantum dots, becomes possible, while avoiding thermal damage [59, 62].

An additional advantage in plasmonic optical tweezers comes from the fact that the evanescent fields can be concentrated beyond the diffraction limit [64]. This near-field trapping provides several benefits comparing with conventional optical tweezers, not only for reducing the trapping scales but also for preventing the damage to the trapped particle with the use of smaller optical intensities [58].

1.5.3 Other techniques

A distinct line of research is focused on exploring different geometries and cavities to achieve optical trapping while seeking the enhancement of the sensing capabilities, such as using devices supporting Whispering-Gallery-Mode (WGM). In these, the guided optical wave supported by total internal reflections drives itself coherently, returning in phase after each revolution. WGM devices combine the generation of evanescent field, that can trap a target particle, with the cavity-based sensors capabilities, that can go down

to the single molecule level [65]. WGM resonators can be presented in different geometries, depending on the target and the system itself. For example, microtoroid optical resonators were used to perform label-free detection. As light circulates in the microtoroid, the evanescent field interacts various times with small analytes that bind to its surface [66]. Moreover, optical resonators such as microspheres have been used to perform the individual detection of virus particles [67].

Other similar technique, known as the carousel trap, is able to attract individual nanoparticles to the sensing volume and they appear to circumnavigate in the direction that light is traveling. Thus, particle sensing can occur due to fluctuations in the resonance frequency and that provides a way for determining the particle size/mass [68].

1.6 Project motivation and objectives

Since the appearance of biosensors, many researchers from different fields, such as photonics, physics, biology and chemistry, gathered to design increasingly sophisticated biosensing devices. The search for further reliable biosensing devices is growing, focusing on more efficient treatments and more timely prevention of certain diseases, such as cancer and Alzheimer disease [6, 69]. With that in mind, some configurations have been described for the purpose of simultaneous trapping and sensing, in order to contribute for biomedicine, where the ability to analyze single cells is paramount [35].

Recent results at the Center of Applied Photonics (CAP) at INESC TEC demonstrate the suitability of optical tweezers as tools that can select and analyze single cells. Optical fiber tweezers combined with backscattered signal analysis and machine learning strategies, allowed for high accuracy discrimination and quantification of different cells and nanostructures.

In this work, we focus on a standard optical tweezers system, where the forward scattered signal is collected using a position sensitive quadrant photodetector. In particular, the goal is to evaluate to which extent can the sensitive position information contribute for a faster and more accurate analysis of the trapped bodies. The vision behind this dissertation is supported by the trapping and sensing of microparticles and cells that allow leveraging on methods of low computational footprint, towards alternative methods for faster classification in today's research.

In order to accomplish this challenging project, the objectives were organized into the following main tasks:

- Optimize the optical tweezers setup:
  - Tune and align all the components;
  - Optimize the data acquisition and processing;
- Explore the performance of the quadrant photodetector:
  - Characterization of position and stiffness constants;
  - Characterization of the optically trapping forces;
- Classification of particles and cells based on the position fluctuations:
  - Classification of different classes (size and composition);
  - Comparison of the results with a fiber-based detection system.

1.7 Structure of the document

This dissertation is organized in six chapters, with the following contents:

Chapter 1, presents a brief context with a review of the state of the art of the evolution of optical tweezers, particularly the applications in the biological field. Moreover, the project motivation and the respective project objectives are presented.

Chapter 2, introduces the physical model of optical tweezers, explaining the origin of the optical forces, which depend on the experimental conditions. A brief introduction to three dimensional optical trapping is discussed, where some system limitations are explored. Additionally, an introduction to Brownian motion is given along with the theoretical procedures necessary to compute the optically trapping forces.

Chapter 3, describes the conventional optical tweezers system used for the experimental procedures. The system characterization is addressed, namely the quadrant photodetector and the corresponding laser based position detection working principle. In addition to the characterization of the system, the calibration of the quadrant photodetector is also presented.

Chapter 4, characterizes the Gaussian beam profile and depicts the experimental results obtained for the calibration of the quadrant photodetector. Additionally, the experimental force measurements are presented, namely the stiffness constant determination. Moreover, the discussion of the results obtained is presented.

Chapter 5, introduces the classification algorithms and procedures used for the classification of particles and cells. In particular, we introduce a novel pre-processing procedure for the extraction of relevant features that is able to perform classification at higher speed rate than those reported in the literature.

Finally, in **Chapter 6**, the future work regarding the optical tweezers experiments conducted in this master dissertation is presented. Additionally the final conclusions are presented.

1.8 List of contributions

Over the duration of this research work two research articles were published in peer reviewed international scientific journals.

Articles in International Scientific Journals:

- Inês A. Carvalho, Nuno A. Silva, Carla C. Rosa, Luís C. C. Coelho, and Pedro A. S. Jorge. Particle Classification through the Analysis of the Forward Scattered Signal in Optical Tweezers. Sensors, 21(18):6181, 2021.

- Pedro A. S. Jorge, Inês A. Carvalho, Filipe M. Marques, Vanessa Pinto, Paulo H. Santos, Sandra M. Rodrigues, Simão P. Faria, Joana S. Paiva, and Nuno A. Silva. Classification of optically trapped particles: A comparison between optical fiber tweezers and conventional setups. Results in Optics, 5:100178, 2021.

Chapter 2

Principles of Optical Tweezers

This chapter aims at presenting an overview of the fundamentals of optical tweezers. First, we describe the basic theory of optical trapping along with the two fundamental regimes, the ray-optics regime and the dipole approximation regime. Then, a discussion regarding the trapping in three dimensions is addressed jointly with the limitations of the technique, namely the diffraction limit and the trapping potential imposed by the system. Finally, we present the methods that will be employed in the subsequent chapters for the determination of the stiffness and force, together with a brief introduction to the theory of Brownian motion.

2.1 Physical model of optical tweezers

In 1986, Ashkin demonstrated for the first time that a single and tightly focused laser beam was able to hold a particle near its focal spot. Such highly focused beam was accomplished with an objective lens of high numerical aperture, capable of bending the light rays towards the focal region focusing the laser to a diffraction-limited spot [4, 10]. These days, typical optical tweezers setups allow the trapping and manipulation of specimens within size ranges of 0.1–10 μm [1], by generating forces of the order of the picoNewtons from just a few milliwats of laser power [4].

An optically trapped particle experiences a change in momentum derived from the reflection and refraction of the trapping beam, resulting in the balancing between the corresponding forces that tend to restore the bead towards the center of the trap [7]. To be precise, the optical force is usually described by two components - the scattering force and the gradient force. The origin of the optical force can be explained differently depending

on the experimental conditions [2]. Although the scattering force usually dominates, it can be challenged by a steep intensity gradient, like the one observed near the focus of a laser beam, thus allowing to balance the two forces [4].

Considering that the target particle has a refractive index higher than the surrounding medium, the behaviour of the focused laser beam can be modeled as an attractive three-dimensional potential well. When the trapped particle experiences a displacement from the equilibrium position, that is, near the focus, a restoring force acts to bring the particle to its equilibrium position. In the most typical conditions, the force in each dimension is reasonably approximated as proportional to the displacement, as given by the Hooke's law [10], as:

$$F_x = -k_p^x(x - x_{eq}) \tag{2.1}$$

where x_{eq} is the position of the particle in equilibrium, x is the particle position, and k_p^x is the trap stiffness [10]. From this model, the trapping potential is then approximated to an harmonic potential [34] given by

$$U(x) = \frac{1}{2}k_p^x(x - x_{eq})^2 \tag{2.2}$$

Regarding the physical origin of the optically-induced forces, we can highlight two fundamental regimes depending on the size of the particle relatively to the wavelength of the trapping laser beam [2]. The ray optics regime, also called as Mie scattering regime, is valid for trapped particles with radius (a) much larger than the wavelength of the trapping laser (λ). Given that, the transfer of momentum to the trapped particle can be obtained through simple ray optics, being this regime valid for $a \gg \lambda$. On the other hand, for particles with radius (a) much smaller than the wavelength (λ) of the trapping laser, the Rayleigh scattering regime is considered since $a \ll \lambda$, and the particle is treated as a point dipole. For a particle whose size is approximately the wavelength of the trapping laser, the simple ray optics and the dipole considerations are no longer valid and a more complex theory is required [8]. Additionally, we should refer that non-spherical or non-homogenous particles also require complex models which are out of the scope of this dissertation [10].

To distinguish if a particle is considered as being much smaller or not in comparison to the laser wavelength [10], we introduce a size parameter given by:

$$k_m a = \frac{2\pi n_m}{\lambda_0} a \tag{2.3}$$

where n_m is the refractive index of the surrounding medium, λ_0 is the trapping wavelength in vacuum and a corresponds to the radius of a spherical particle [10].

In typical experiments the trapping wavelength is located in the NIR range, which means that particles within the micrometer range usually belong to the Mie regime [10]. The Mie scattering regime is thus valid when the size parameter is much bigger than unity, expressed as:

$$k_m a \gg 1 \tag{2.4}$$

Oppositely, in the Rayleigh regime the particle is approximated to a dipole, and the electromagnetic field inside its volume is considered homogeneous [10]. Then, two parameters must be fulfilled simultaneously to fit this regime, which are given by

$$k_m a \ll 1 \qquad \frac{n_p}{n_m} k_m a \ll 1 \tag{2.5}$$

where n_p represents the refractive index of the particle. The addition of the second condition is relevant for small particles with complex or high refractive index [10].

2.1.1 Ray-optics regime

In the ray-optics regime, the force can be computed from the sum of the reflected and refracted ray components. In short, the reflection and refraction of light results in a change in momentum (Δp) that, accordingly to Newton's 3rd law, imparts an equal and opposite momentum change to the particle [4]. To better illustrate the mechanism, three distinct examples of a dielectric particle irradiated by two incident light beams are presented and described in detail in Figure 2.1.

The first and second geometrical cases represent the possible positions of the particle on the optical axis, relatively to the focal region [6, 8]. In the first example, case (A), the particle is located below the focus, which is represented in the intersection of the dotted lines. The reflected rays are responsible for the scattering force (defined as F_{scatt}, colored in orange) while the refracted rays are responsible for the gradient force which acts in the opposite direction, balancing scattering towards the focus spot (defined as F, colored in black) [6, 8]. In case (B) a particle located above the focus is represented, with both scattering and gradient forces driving the particle in the direction of the focal spot. In its turn, case (C) represents a particle out of the laser beam optical axis, hence a transverse field gradient is presented, and part of the particle will be subject to a greater intensity, meaning that the intensity of **ray b** will be greater than the intensity of **ray a**.

A perturbation to the right relatively to the the incident laser, causes a leftward-directed force back towards the focus. Once again, the particle will be redirected towards the highest power region of the laser, that is, the center of the Gaussian light distribution [6, 8].

Although the resulting forces depend on the position of the bead, it is conceptually accepted that the gradient force tends to restore the bead towards the focus position, while the scattering force points in the direction of the light beam propagation [6, 8]. Moreover, while secondary scattering events also occur, the optical forces are mostly associated with the first two scattering events, that is first reflection of the beam and the first transmission through the particle, which was taken into consideration in the ray-optics regime [10].

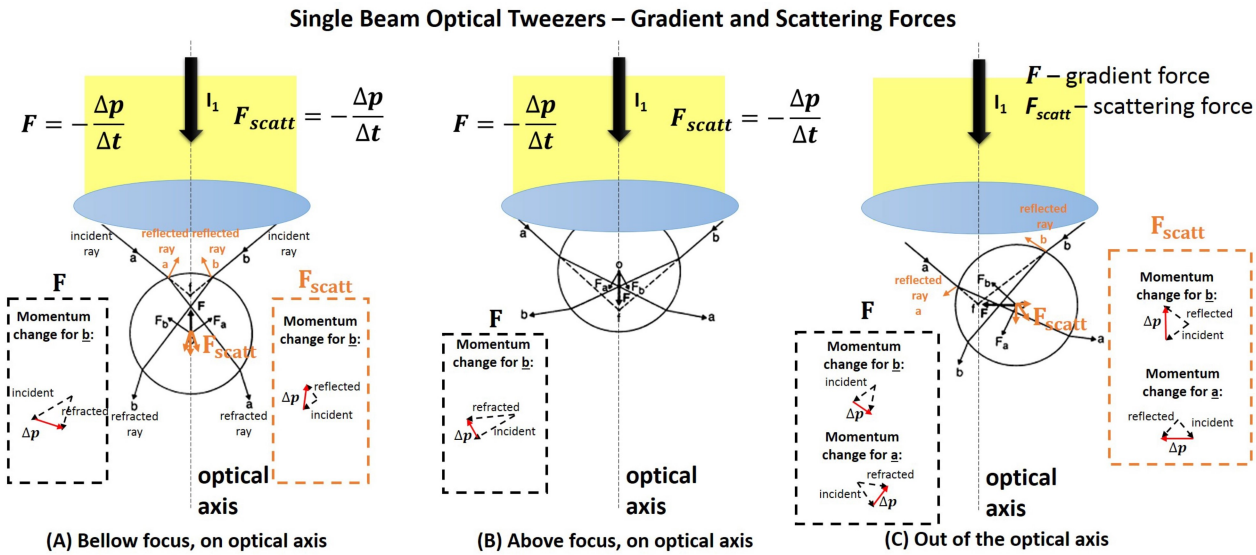

FIGURE 2.1: Geometrical scheme representing different situations in Mie's Regime. Description of forces acting on a particle located (A) bellow the focus, (B) above the focus and (C) displaced from the optical axis [6].

2.1.2 Dipole approximation regime

For a particle in the Rayleigh regime, or the dipole approximation regime, the total optical force divides once again in two distinct components [2, 8]. The scattering force arises from the process of absorption and re-emission of light by the trapped dipole particle [4]. The scattering component is thus proportional to the optical intensity and tends to push the particle in the direction of the propagation of the incident light [2, 4]. For a spherical particle, the scattering force is expressed as:

$$F_{scattering} = \frac{(I_0 \sigma n_m)}{c} \tag{2.6}$$

where I_0 represents the intensity of the incident light (trapping laser beam), σ is the scattering cross section of the sphere and c is the speed of light (in vacuum) [4]. The scattering cross section can be given by

$$\sigma = \frac{128\pi^5 a^6}{3\lambda^4}\left(\frac{m^2-1}{m^2+2}\right)^2 \tag{2.7}$$

where λ is the wavelength of the laser beam and m is the ratio between the index of refraction of the particle and the medium ($m = n_p/n_m$). That said, it can be observed that the scattering component is proportional to the optical intensity, to the particle scattering cross section and also depends on the size of the particle [4].

On the other hand, the gradient force results from the spatial variation of the optical intensity and is experienced by a dipole when immersed on an non homogeneous electric field [4]. The gradient force is proportional to, and acts in the direction of, the intensity gradient [2], as given by:

$$F_{gradient} = \frac{2\pi\alpha}{cn_m^2}\nabla I_0 \tag{2.8}$$

where α represents the polarizability of the microsphere and ∇I_0 is the gradient of intensity of the incident light [4]. The polarizability of the particle is given by:

$$\alpha = n_m^2 a^3\left(\frac{m^2-1}{m^2+2}\right) \tag{2.9}$$

As in the ray optics regime, a stable trapping is only achieved if the scattering and the gradient components cancel each other. However, if we analyze the radius dependence of each component we observe that the scattering force is proportional to the sixth power of the particle radius a^6 while the gradient force is proportional to the third power of the particle radius a^3. Thus, we can conclude that when the size of the specimen is reduced towards the nanoscale, the scattering force becomes predominant and at some point is no longer possible to trap the particles with a standard optical tweezers system.

Additionally, we remark that not only the size of the particle affects the efficiency of the trapping phenomenon, but also their intrinsic properties, such as the refractive index and the absorption of the particle for a particular incident radiation [14]. For example, trapping with Gaussian beams can only be achieved when the refractive index of the particle is greater than the refractive index of the surrounding medium at the trapping wavelength. Otherwise the particle will be pushed away from the center of the trap.

Moreover, if the particle is too absorptive, additional effects such as thermal dissipation, can become relevant, causing damage to the particles and cells [70, 71].

2.2 Optical trapping in three dimensions

In optical tweezers using a single Gaussian beam, the spatial inhomogeneity of the electric field of the incident laser generates a gradient trapping force towards the focus spot. If the gradient is sufficiently steep, the axial component of the gradient force can dominate the axial stability, balancing the scattering force in regions of zero net force, as seen in Figure 2.2, enabling three dimensional stable optical trapping [1, 2, 4]. Moreover, we shall note that the equilibrium position in the axial direction for a trapped particle is not located exactly at the focal point, but at a small distance beyond that, in a location where the backward gradient force has the same magnitude but opposite direction as the scattering force [4].

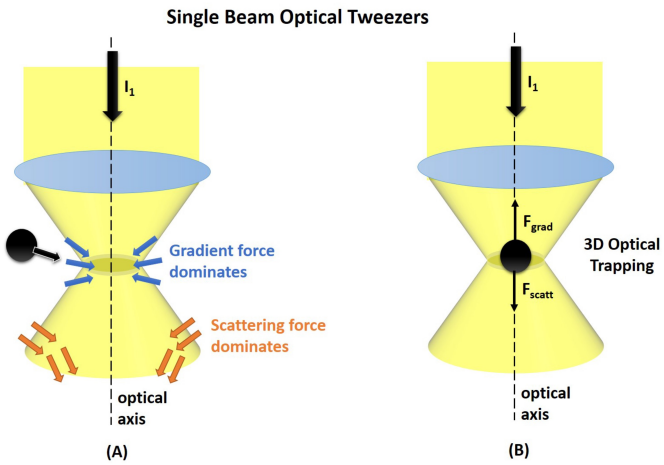

FIGURE 2.2: Scheme representing the optical forces in a single beam optical tweezers configuration. (A) Single beam optical tweezers configuration where the axial gradient component of the force dominates the axial stability for three dimensional optical trapping. (B) Single beam optical tweezers configuration where the axial component of the gradient force exceeds the scattering component. The location of zero net force is positioned a little beyond the focal point [6].

In the transverse axis, the Gaussian beam is characterized by an intensity profile $I(r)$ that exhibits a bell-shaped curve as can be observed in Figure 2.3. This intensity profile is symmetric around the central peak and varies along the optical axis of the beam. Indeed, the farther from the focus region, in the z-axis direction, the smaller is the peak intensity. Additionally, the beam radius represented by $w(z)$ also changes along the beam

propagation direction, with the minimum radius known as beam waist w_0 being located at $z = 0$, while the Rayleigh range z_R characterizes the beam radius located at $w(z) = \sqrt{2}w_0$. Moreover, to estimate the beam radius for a given axial displacement one can employ $w(z) = w_0\sqrt{1 + z^2/z_R^2}$. As expected, the smaller the beam waist created, the smaller is the Rayleigh range and consequently the larger the beam divergence Θ [72, 73].

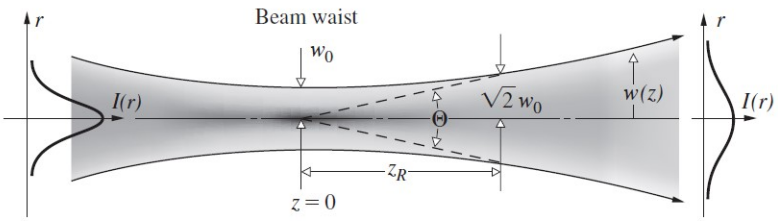

FIGURE 2.3: Spreading of a Gaussian beam. The intensity profile is represented in two locations of the z-axis, along with all the constants that characterize the Gaussian beam behavior [73].

While we focused our attention on the case of a Gaussian beam, we shall also note that stable optical trapping can be attained in other configurations by exploring many distinct mechanisms. For example, the most typical counter-propagating laser beam configuration, that employs two trapping beams, achieves stable trapping through the balance of the axial scattering forces which cancel each other, while the gradient components capture the particle using the interference pattern created by the two counter propagating laser beams [7]. Another interesting example is the case of the optical levitation trap, a trap that appeared before single beam optical tweezers, where the axial stability was attained with the balance between the scaterring component and gravity [2].

On a conventional optical tweezers system, the manipulation and visualization of particles in the nanometer scale is constrained by the diffraction limit associated to the focusing of the trapping laser beam by a microscope objective. In the far-field regime of light propagation, the maximum spatial resolution is thus set by diffraction. Depending on the numerical aperture of the microscope objective lens, the wavelength of the incident radiation, and the refractive index of the medium, the minimum spotsize $\triangle x$ in which we can focus light [1] is determined from the Rayleigh criterium, given by

$$\triangle x = \frac{1.22\lambda}{NA} \tag{2.10}$$

where NA is the numerical aperture of the objective lens.

Considering our optical tweezers system, the resolution can be computed by equation 2.10. Hence, objects smaller than the diffraction limited spot of 0.952 μm can not be resolved or discriminated.

The concept of near field optics emerged as a way to overcome the diffraction limit of optical resolution, and the lack of stability when attempting to trap nanoscale specimens, as described in section 1.5.

2.3 Trapped particle dynamics and force computation

To calibrate an optical tweezers system and accurately measure optical-induced forces, precise position determination and stiffness calibration must be assured. For this purpose, we can study the trapped particle dynamics to establish the relation between the physical model and the experimental observations, providing accurate calibration of the system as presented in the subsequent sections.

2.3.1 Theory of Brownian motion

From a microscopic perspective, a particle with a size comparable to that of the molecules of the immersion fluid is permanently moving in random directions. This characteristic movement, known as Brownian motion, occurs in a solution due to the collisions between the solute particle with medium molecules [10, 74]. Usually described as a random walk, the trajectory changes at the microscopic scale can ultimately be related with the viscosity of the medium observed at the macroscopic level.

To illustrate this fact, we introduce the physical model for the motion of a free Brownian particle immersed in a fluid [74], which is given by the Langevin equation

$$m\ddot{\boldsymbol{r}}(t) = -\gamma\dot{\boldsymbol{r}}(t) + \sqrt{2k_BT\gamma}\boldsymbol{W}(t) \tag{2.11}$$

where m is the mass of the immersed particle, $\boldsymbol{r}$ represents the vector position of the particle, γ is the particle friction coefficient, k_B is the Boltzmann constant, T is the absolute temperature and $\boldsymbol{W}(t)$ is a stochastic vector term accounting for random collisions [10, 74]. Furthermore, we note that the first term on the right-hand side of equation 2.11 can be related to the drag force felt by a spherical particle of radius a, as given by the Stoke's law

$$\gamma = 6\pi\eta a, \tag{2.12}$$

thus establishing the relation between the microscopic dynamics and the viscosity of the medium η.

In the presence of the a trapping potential, the model for the Brownian particle shall include an additional deterministic contribution of the optical-induced force [10, 75], which results into

$$m\ddot{\boldsymbol{r}}(t) = -\gamma\dot{\boldsymbol{r}}(t) - \boldsymbol{k}_p \odot \boldsymbol{r}(t) + \sqrt{2k_B T\gamma}\boldsymbol{W}(t) \tag{2.13}$$

where k_p is the trap stiffness constant represented as a vector (k_p^x, k_p^y, k_p^z) and $\odot$ stands for the Hadamard product.

Typically, optical tweezers exploit systems of low Reynolds number, allowing to drop the inertial term $m\ddot{r}$ [10, 75] in equation 2.13. The result is an over-damped Langevin equation given by

$$\gamma\dot{\boldsymbol{r}}(t) + \boldsymbol{k}_p \odot \boldsymbol{r}(t) = \sqrt{2k_B T\gamma}\boldsymbol{W}(t) \tag{2.14}$$

which simplifies the modelling of the dynamics of the trapped particles.

Before advancing we call the attention to the fact that this model is also useful to provide an insight and lower bound to the depth of the optical potential. As already discussed, distinct materials and sizes result into distinct optical trapping potentials, an idea illustrated in the example provided in Figure 2.4. We can see that distinct particle sizes result in distinct spatial probability density distributions, which means that a stronger and a looser confinement are associated with higher and lower absolute values of the trapping potential, respectively. Indeed, a stronger confinement leads to a thinner distribution around the equilibrium position, whereas a weaker optical trap results in a wider distribution, meaning that it is easier to escape the optical trap in the second situation. Studying the properties of the resulting distribution, it can be argued that for the case of a Gaussian beam, a potential well of depth $\approx 10\ k_B T$ is the lower bound necessary to overcome Brownian motion and stably confine the particles inside the trap [1, 10, 64].

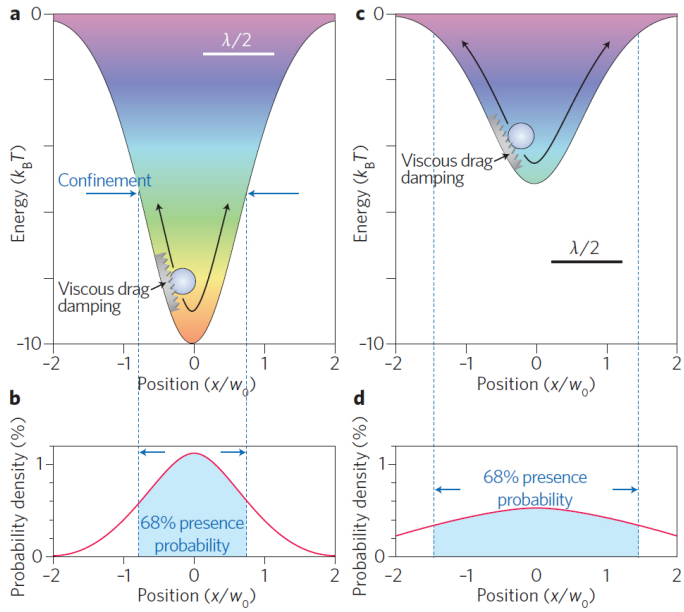

FIGURE 2.4: Representation of the harmonic potential for conventional optical trapping. The upper left figure, figure **a**, represents the trapping potential, and below, in figure **b**, it is represented the position distribution, where both are related to the analysis of a trapped polystyrene particle of radius R. The upper right figure, figure **c**, represents the trapping potential, and below, in figure **d**, it is presented the position distribution, and both related to the analysis of a trapped polystyrene particle of radius 0.8R [64]

Understanding and observing the physics of Brownian motion in an optical trap allows to experimentally probe physical properties of the trapped bead, including the optical forces acting on it [4]. As described in section 1.3.2, these dynamics can be used as passive methods for the determination of the optical force and calibration of the system. In the subsequent sections we introduce three passive approaches used to compute and characterize the optical force: i) the equipartition method, ii) the power spectral density method and iii) the Boltzmann statistics method.

2.3.2 Equipartition method

The equipartition method explores the connection between the dynamics of the macroscopic world with the particles and atoms of the microscopic world, as described through the laws of thermodynamics. To be precise, a trapped particle in an harmonic potential has a potential energy given by $\frac{1}{2}k_x <(x - x_{eq})^2>$, where the particle position distribution corresponds to a Gaussian distribution [29, 34]. Using the Equipartition theorem, that states that at thermal equilibrium each degree of freedom has a mean energy of $\frac{1}{2}k_B T$ due to the thermal fluctuations, it is straightforward to obtain that [4, 29]

$$\frac{1}{2}k_p^x \left\langle \left(x - x_{eq}\right)^2 \right\rangle = \frac{1}{2}k_B T \tag{2.15}$$

where $<(x - x_{eq})^2>$ corresponds to the statistical variance of the particle position derived from the fluctuations over time [29, 76]. As expected, at thermal equilibrium, i.e., where $K_B T$ constant, the higher the stiffness constant, the smaller the statistical variance of the particle position, which aligns with the discussion of the previous section.

The advantage of the equipartition method is the fast and simple computational procedure, only requiring the recording of the position of the trapped particle over time [4, 29], what is easily achieved by using a quadrant photodetector. However, to compute the stiffness, a previous position calibration of the quadrant photodetector is necessary. In addition, the method also features some caveats, as it is unable to compute the friction properties of the particle, needed to achieve a complete and precise characterization of the system.

2.3.3 Power spectral density method

The power spectral density (PSD) method lays on the analysis of the power spectrum of the fluctuations of a trapped particle [29]. Considering the low Reynolds number regime discussed in section 2.3.1, it is straightforward to obtain the one-sided power spectrum $S(f)$ of the fluctuations of a trapped particle [4, 29] as a Lorentzian function given by

$$S_{xx}(f) = \frac{k_B T}{\pi^2 \gamma (f_0^2 + f^2)} \tag{2.16}$$

where f stands for the frequency. The characteristic roll-off frequency f_0, also referenced as corner frequency is related to the properties of the optical trap and of the particle. This way, the stiffness constant is computed by

$$k_p^x = 2\pi\gamma f_0. \tag{2.17}$$

By fitting the power spectrum to a Lorentzian function, both the corner frequency and γ can be extracted [29, 77], and from these the trap stiffness can be estimated.

Unlikewise the Equipartition method, the PSD method provides additional information on the particle friction parameter. Furthermore, it is independent on calibration factors.

2.3.4 Boltzmann statistics method

The main advantage of the Boltzmann statistics method is that it does not require the trap potential to be harmonic, as in the previously described methods. Hence, this methods allows to better probe the geometry of the trapping potential and to characterize the system. In short, the method explores the laws of statistical mechanics and the distribution of a classical system over various energy states in thermal equilibrium to characterize the optical potential.

Assuming the action of a conservative force, i.e. $F_x = -\frac{dU(x)}{dx}$., the probability density $\rho(x)$ of the particle position (x) can be described as a function of the trapping potential $U(x)$ [10, 34] as given by the Boltzmann distribution

$$\rho(x) = \rho_0 e^{\left(-\frac{U(x)}{k_B T}\right)} \tag{2.18}$$

where ρ_0 is a constant normalization [29].

Experimentally, this distribution can be computed by analysing the position of the trapped particle and constructing the corresponding histogram, which approximates the probability density function, $\rho(x)$. The optical potential can be obtained by inverting equation 2.18 for the equilibrium potential $U(x)$ [10, 34], which results into

$$U(x) = -k_B T ln \frac{\rho(x)}{\rho_0} \tag{2.19}$$

This methodology does not require information on medium viscosity or particle radius to determine the trap stiffness constant, and remains valid in geometries other than the harmonic potential created by a typical Gaussian beam trap [10, 34]. Even so, it can be used to estimate the stiffness constant, by fitting an harmonic function to the resulting potential curve.

2.4 Concluding remarks

In this chapter, the fundamental aspects of optical trapping have been described, along with the main limitations regarding conventional optical tweezers systems. The optical force methods employed in this thesis project to characterize the optical tweezers system have been detailed, with a particular focus on the stiffness constant determination resulting from the particle dynamics, which will be fundamental in the subsequent chapters.

Chapter 3

Experimental setup: characterization and calibration

A fundamental part of the activities of this dissertation is the assembly and calibration of a conventional optical tweezers system. This chapter reports these efforts, starting with considerations on the setup and a brief description of the system alignment. After that, we describe the working concepts of some important system components, highlighting the laser-based position detection system with the quadrant photodetector. Finally, we present the experimental protocol used to prepare the samples, and the produced 3-D sample holder, employed throughout the experimental activities.

3.1 Description of the experimental setup

In this work we used a standard optical tweezers system (OTKB - Modular Optical Tweezers System, Thorlabs, USA) depicted in Figure 3.2. This system explores an inverted microscope configuration mounted on an optical table, with schematic given in Figure 3.1. A fiber laser diode (Lumentum s27-7602-460, consult section A.1 from Appendix A for laser specifications) with a continuous emission at 976 nm and a maximum output power of 460 mW is coupled into a 980 nm single mode optical fiber (SM 980-5.8-125, Thorlabs). The collimated laser beam is reflected through the system, reaching a Galilean beam expander, which is composed by achromatic doublets, characterized by a focal length of -50 mm and +150 mm. The beam expander minimizes the overall space and provides an expansion factor of approximately 3, which is essential to assure the maximum filling of the back aperture of the objective lens ($\approx$10 mm) thus approaching a diffraction limited

performance, and creating a stronger trap. Following that, the laser beam is directed to the 100X oil immersion objective (E Plan 100x/1.25 Oil, Nikon) that focuses the beam to an estimated focal spot of 1.1 μm onto the sample, creating the optical trap.

After passing through the sample, the transmitted laser is recollimated with a 10x air condenser lens (E Plan Achromat 10X, Nikon) and the dichroic mirror redirects the beam towards a quadrant photodetector (PDQ80A, Thorlabs) placed at a conjugate back focal plane of the condenser lens. To ensure that the condenser lens and the objective lens were positioned in the correct location in respect to the focal plane, the microscope objective was placed at approximately 7 mm from the condenser lens.

A positioning stage is connected to the cube modules, being useful for the manipulation of the sample holder which contains the sample. Following that, the neutral filter and the 40 mm lens are placed on XY cage adjusters. The cage adjusters allow movement of ± 1 mm perpendicularly to the optical axis. Their positioning with respect to the detector can be useful to precisely center the laser spot onto the detector by fine adjustment. In addition, the 40 mm lens is responsible to image the back focal plane of the back aperture of the condenser lens onto the detector, while the neutral filter, with optical density of OD=0.6, is essential for preventing detector saturation.

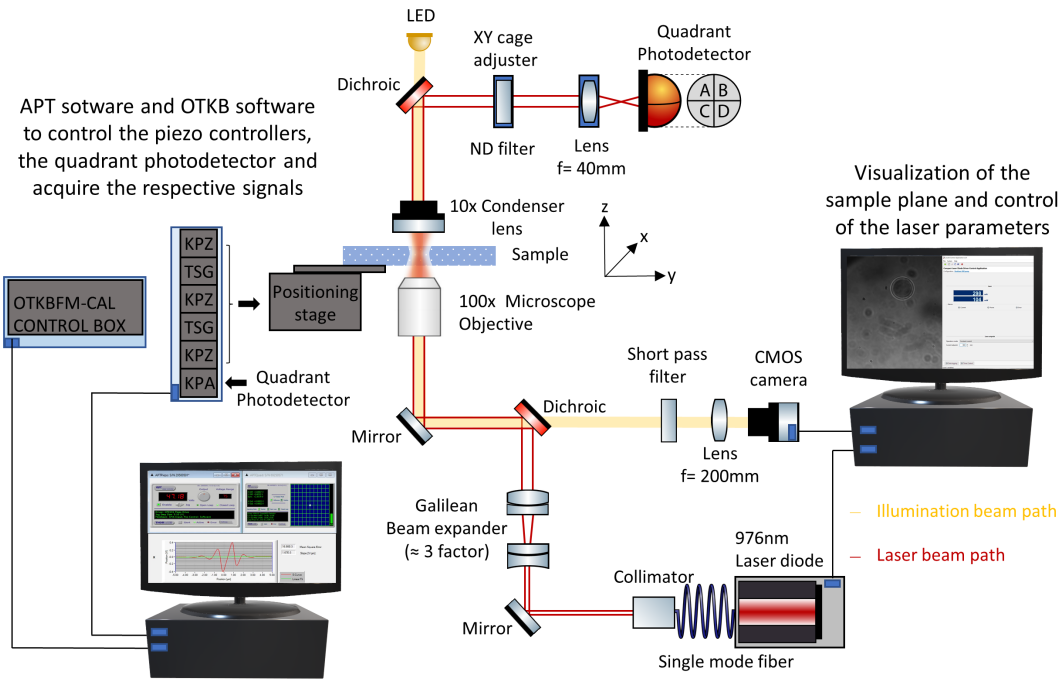

FIGURE 3.1: Schematic of the conventional optical tweezers system and the respective instrumentation required for the control of the optical trapping phenomenon. The red tracing represents the trapping NIR light circuit while the yellow shade represents the sample imaging circuit.

The 100X oil immersion objective is used both for trapping and imaging the sample and the immersion oil used has a refraction index of ≈1.5. The sample is illuminated by the LED at the top and the respective image is captured by a 1280x1024 color CMOS camera (DCC1240, Thorlabs). To prevent the damage of the camera, a shortpass filter is placed with a cut-off wavelength of 750 nm, and a 200 mm focal length achromatic lens is used to image the sample plane. The trapping events in the plane of the specimen can thus be monitored and recorded by the Thorcam software (Thorlabs). Additionally, it is also possible to perform particle size measurements on the image acquired by using the magnification provided and the pixel size. We use the pixel size conversion, in which one pixel corresponds to 5.3 μm in the magnified image, resulting from the 1.25 NA 100X microscope objective. With the correct positioning of the optical tools regarding the imaging system, we can ensure that the magnification of the acquired image is only caused by the amplification factor of the microscope objective [73].

3.1.1 Additional modules and controllers

The addition of external modules to the conventional setup allows to control the system and acquiring the data related to the position fluctuations of the particle. For data acquisition, three modules are available, the K-cube piezo controller (KPZ), the T-cube strain gauge reader (TSG) and the K-cube beam position aligner (KPA). The piezo actuators allow local and computerized displacement along a single direction through high voltage operation. Conversely, the strain gauge readers are responsible for reading the position displacement for a particular axis. The piezo controller cubes and the strain gauge cubes can be used to monitor the three dimensions and the displacement itself can be controlled by an open or closed loop operation mode. In open loop operation, the displacement read may not correspond to the one initially demanded, while in closed loop operation mode, the error between the displacement demanded by the piezo controllers and the position displacement measured decreases, allowing better control of the system. Additionally, the beam position aligner cube allows monitoring of the signals that derive from the quadrant photodetector, which will be further explored in section 3.2.1.

The USB Controller Hub and Power Supply device (KCH601) is connected to a power supply and is used to power up individually the three cube modules minimizing the USB connections necessary. The positioning stage is also connected to the cube modules, with exception of the KPA cube module, which is connected to the quadrant photodetector. The

positioning stage provides 20 μm of displacement in all three directions with 20 nm of positioning precision. In addition, a data acquisition card (USB6212, National Instruments), often represented by OTKBFM-CAL control box, is connected to the cube modules. The data acquisition card connects to a power supply, and acquires the channels from the detector, enabling fast stage positioning. After all connections are made, the control of the positioning stage and the cube modules can be accomplished with the APT software (Thorlabs). Moreover, for calibration purposes and to record the position fluctuations the OTKB software (Thorlabs) is used.

To control the stability of the optical trapping process, the laser parameters configured in the CLDD software were monitored over time, in particular the TEC temperature variation to avoid damage to the diode laser. The laser was set to operate in constant average current mode, where the laser current is maintained at a constant value. The setpoint, defined in CLDD software, enables the control of the optical power by the laser current defined.

In this system, the maximum optical power accessible in the sample plane is close to 120 mW considering 1000 mA as the maximum current. According to the manufacturer, the losses due to the microscope objective are approximately 26.25% at 976 nm. Although the wavelength of the trapping laser is located near the infrared region, where there is a low absorption of light, the experimental measurements were conducted at optical powers much lower than the maximum power available, to avoid temperature instability and thermal dissipation, which can damage particles and cells.

3.1.2 System alignment and laser power calibration

The precise alignment of the laser beam through the system modules is necessary to warrant the expected performance and stability of the system. To accomplish this in a safe and successful way, several accessories were used, including a power meter (PM100D, Thorlabs) with a thermal power sensor head (S302C, Thorlabs), operating at a correction wavelength of 976 nm, laser safety glasses, a laser sensible target, a laser viewing card, and an infrared viewer (FIND-R-SCOPE 84499A). Particularly, in the vertical alignment of the laser beam, low optical power was set, and the use of safety glasses was mandatory for safety reasons. Along the alignment process, the viewing card, the laser sensible target and the infrared viewer were useful to guarantee the alignment and the collimation of the laser beam.

Additionally, the power meter and the thermal power sensor head were used to measure the optical power at the end of the optical fiber for calibration purposes. To characterize the optical power in the sample plane, the optical power was measured before the laser entering the objective lens, for up to 300 mA of laser current. Additionally, the other values were obtained by extrapolation of the trend line. For the determination of the optical power in the sample plane, the losses due to the microscope objective were considered.

In this dissertation, the experimental measurements conducted exploited four different optical powers, 9.870 mW, 22.575 mW, 35.070 mW and 47.502 mW, in the sample plane, controlled by the laser current. Additional information regarding the laser characterization is available in section A.1 from Appendix A.

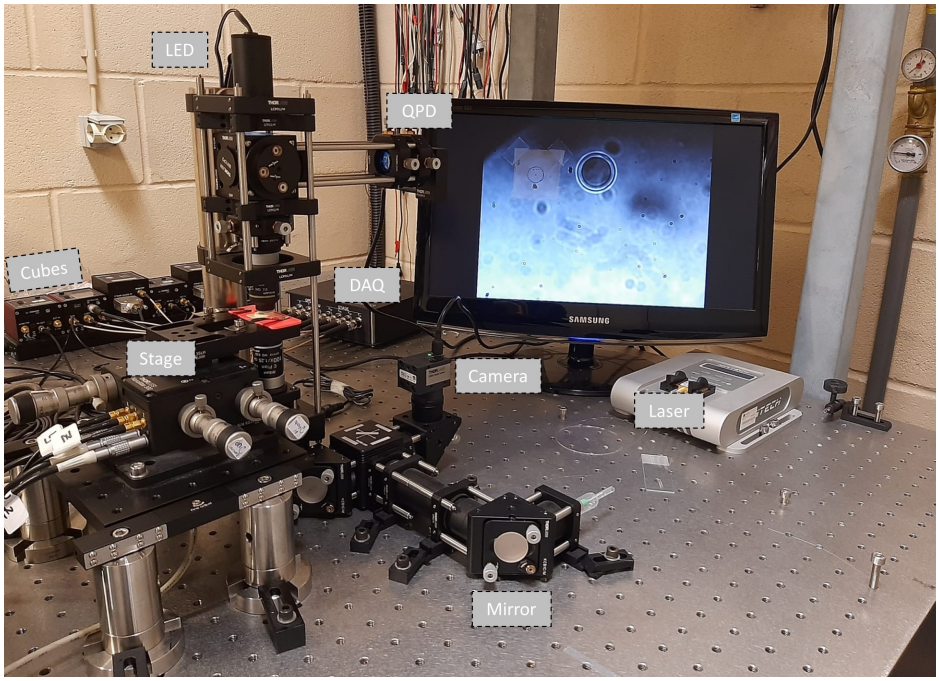

FIGURE 3.2: Conventional optical tweezers system (OTKB) used for trapping and classification of specimens.

3.2 Laser-based position detection

Measuring the change of position of a trapped particle/cell in an optical trap system is essential to determine the stiffness and force acting on it. In our experimental setup we make use of the concept of laser-based position detection and explored the methodology of back focal plane detection, as already introduced in section 1.3.1. Besides characterizing the optical forces, this approach can also be used to calibrate the detector positioning output.

Considering an optical tweezers system, the microscope objective and the condenser lens are placed so that the working distance of both is respected, meaning that, the focal plane of the inverted 100X microscope objective must be in the exact same location as the focal plane of the condenser lens, as seen in Figure 3.3. Following that, the detection principle of the BFP detection lays on the pattern changes in the back focal plane, located oppositely to the object formed in the focal plane of the condenser lens. After passing the condenser lens, the collimated laser beam will be used to detect the pattern changes by placing a 40 mm lens, depicted in Figure 3.4, which will project the object plane onto the quadrant photodetector, forming the image.

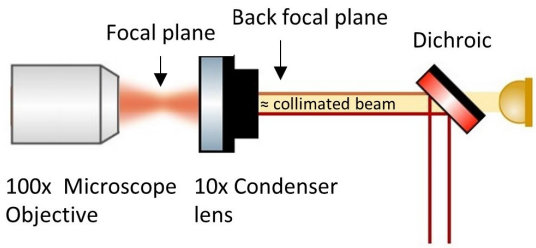

FIGURE 3.3: Schematic of the focal plane and the back focal plane of the condenser lens regarding the conventional optical tweezers system. The beam collected by the condenser lens is collimated and redirected to the quadrant photodetector.

The quadrant photodetector detects pattern changes of the beam deflection angle, which arise from the change of position of the trapped particles [34]. To enable this the optical tools have to be precisely placed, so that the laser spot onto the detector fulfills the requirements, that will be described in section 3.2.1. For that, ImageJ software was used to support the measurement of the distances between the optical tools by capturing a photograph of the system and then measure accurately the distance between the instruments.

As presented in Figure 3.4A, the object distance is represented by So and the image distance is represented by Si. In addition, So is split by two distances, as the optical path is vertical and horizontal. The corresponding distances $o\alpha$+BFP and $o\beta$ were chosen accordingly to the available space in the optical tweezers system. In addition, the focal length of the lens is represented by f, as seen in Figure 3.4B. The distances mentioned above are presented in Table 3.1.

TABLE 3.1: Representation of the distances related to the location of the optical tools in the optical tweezers system and the respective focal length of the lens.

Symbol	So	$o\alpha$+BFP	$o\beta$	f
Distance	14.245 cm	6.245 cm	8 cm	4 cm

The Gaussian lens formula can be used to determine the image distance Si and consequently the size of the laser spot onto the detector can be estimated [73]. The Gaussian lens formula is given by

$$\frac{1}{f} = \frac{1}{So} + \frac{1}{Si} \tag{3.1}$$

where f is the focal length of the lens yielding an image conjugate plane at Si= 5.5617 cm, corresponding to the required distance from lens to the quadrant photodetector.

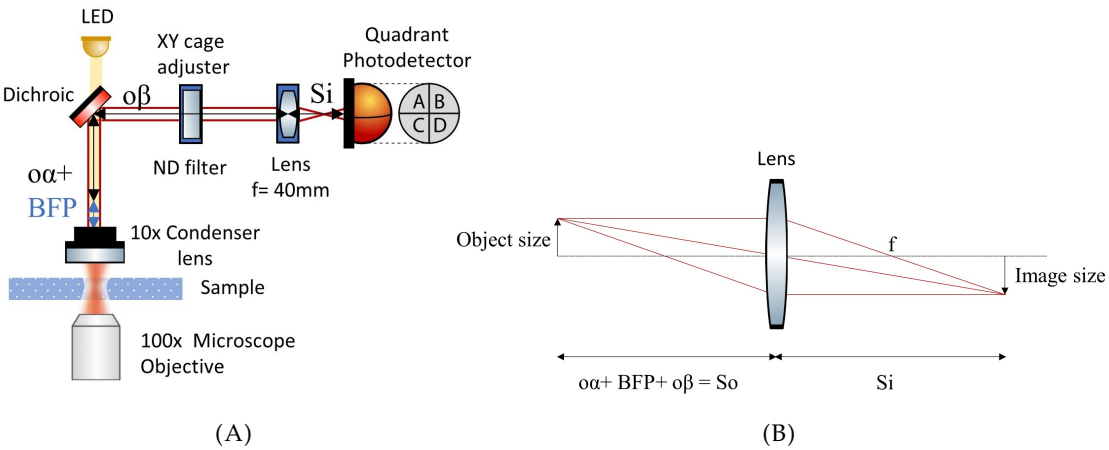

FIGURE 3.4: Schematic of the back focal plane detection in conventional optical tweezers. (A) Schematic of the optical tools placed according to the distances for proper operation of the system. (B) Schematic of ray tracing in a thin lens system.

After setting the QPD position, the next step is the determination of the laser beam diameter at the QPD detection surface from the transverse magnification given by

$$M_T = -\frac{Si}{So} = \frac{\text{Image size}}{\text{Object size}} \tag{3.2}$$

For our system, the condenser BFP aperture is $\approx 8mm$ wide, yielding a spot size at the BFP detection plane 3.084 mm wide, according to equation 3.2. This dimension, as described in the next section, is appropriate for QPD optimal operation.

3.2.1 Characterization of the quadrant photodetector

The quadrant photodetector (PDQ80A, Thorlabs) is a semiconductor silicon photodiode that is divided in four segments separated by a ~ 0.1 mm gap, where each segment corresponds to a quadrant. It operates within the 400-1050 nm wavelength range, with a 0.65 (W/A) responsivity at 976 nm, and is characterized by a 150 kHz bandwidth. The device is capable of detecting beam diameters smaller than 7.8 mm. However, to ensure the best performance, the beam diameter (i) should be adjusted between 1 $mm < i < 3.9$ mm [78]. A schematic of the quadrant photodetector is provided in Figure 3.5.

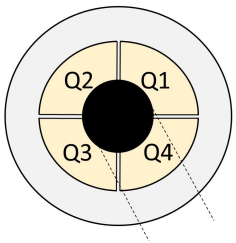

FIGURE 3.5: Schematic of laser beam incident (represented by the black color) onto the quadrant photodetector, where the four quadrants Q1, Q2, Q3 and Q4 are presented (by the yellow color). This schematic is based on reference [78].

The detector is sensitive to the position of the incident beam and its design allows the detection of the deflections of the trapping laser, which derive from the displacements of the trapped particle. The high spatial and temporal resolution allow accurate detection of the position over time [4, 79].

When light hits the detector, a photocurrent is detected in each segment. Usually the detection circuit is based on four steps, the preamplifier stage, the post amplifier, the reciprocal amplifier and lastly the analog-to-digital converter step. The photocurrent detected in each segment is usually small, being proportional to the light intensity. Following that, a trans-impedance amplifier is used to convert the photocurrent to voltage signals [80, 81]. Then, after the respective processing circuit, difference normalized signals representative of positions X and positions Y are acquired as well as an average intensity signal [23].

The difference signals, commonly expressed by X_{Diff} and Y_{Diff} are related to the position of the beam detected in the quadrants. The difference signals are expressed as

$$X_{Diff} = (Q2 + Q3) - (Q1 + Q4) \tag{3.3}$$

$$Y_{Diff} = (Q1 + Q2) - (Q3 + Q4) \tag{3.4}$$

where Q1, Q2, Q3 and Q4 represent the four quadrants present in the detector. The difference between the intensity in the quadrants allows to understand where the beam is positioned, relatively to the horizontal and vertical direction.

The total intensity signal, usually expressed as SUM signal, is used to measure changes in the beam intensity and can be used for normalization purposes to correct possible intensity fluctuations [82]. The SUM is expressed as

$$SUM = (Q1 + Q2 + Q3 + Q4) \tag{3.5}$$

where SUM represents the contributions from all the quadrants.

As mentioned, the total intensity signal can be used for normalization, in particular to normalize X_{Diff} and Y_{Diff} signals. Consequently, the normalized coordinates (X, Y) for the position of the laser beam can be expressed as

$$X = \frac{(Q2 + Q3) - (Q1 + Q4)}{(Q1 + Q2 + Q3 + Q4)} \tag{3.6}$$

$$Y = \frac{(Q1 + Q2) - (Q3 + Q4)}{(Q1 + Q2 + Q3 + Q4)} \tag{3.7}$$

where the numerator corresponds to the X_{Diff} signal and Y_{Diff} signal and the denominator is the SUM signal.

In essence, the quadrant photodetector retrieves three signals, the $XDiff$ normalized signal, the $YDiff$ normalized signal and the SUM signal. When a symmetric beam is perfectly centered onto the detector, the photocurrents will be the same in each quadrant. The difference between the left and the right side (for X signal) and the difference between the top and the bottom (for Y signal) is approximately null and a value close to zero output voltage is displayed, for a perfectly centered beam [76, 78, 82].

The displacement in the horizontal orientation, that is, in the x direction is considered to be positive when placed on the left side relatively to the center of the photodiode array and negative when placed on the right side (as seen in Figure 3.6). This positive and negative values for horizontal displacement can be derived from equation 3.6. Additionally, the displacement of the beam vertically, in the y direction is considered to be positive when placed above the center, on the top region relatively to the center of the photodiode array and negative when place below the center of the axis, on the bottom. This positive and negative values for vertical displacement can be derived from equation 3.7.

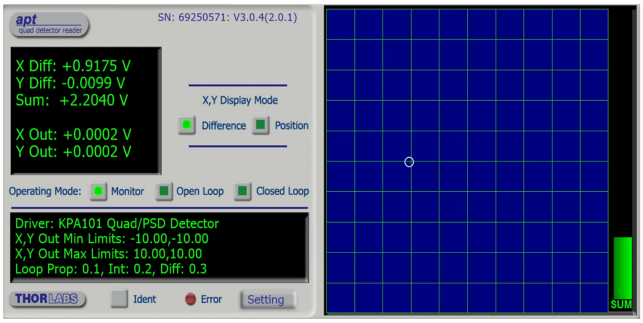

FIGURE 3.6: Position aligner APT software GUI. Signals acquired from the quadrant photodetector when the beam is displaced in the positive horizontal direction, through fine adjustment. In X,Y Display Mode, Difference is selected so that the display plots the $XDiff$ and $YDiff$ signals from the array. The white circle displayed represents the position of the center of the laser beam on the detector.

The $XDiff$ and $YDiff$ normalized signals can be converted into distances, with the detector conversion factor assuming that the distance of the trapped particle to the center of the trap is located in a linear range of variation. Furthermore, this calibration requires a precise alignment of the laser beam in the horizontal and vertical direction onto the detector, as well as the proper alignment of the center of the laser beam in the center of the photodiode array, with fine adjustment (XY cage adjusters).

The real displacement of the particle relatively to the center of the trap is thus given by

$$< X_{QPD} > =< (V_{QPD} \times S_{QPD}) > \tag{3.8}$$

where X_{QPD} corresponds to the changes in position, encoded by the deflections of the beam. This information can be obtained by applying an adequate calibration factor S_{QPD}, to the voltage signals V_{QPD} yielded by the QPD outputs. From dimensional analysis it is straightforward to conclude that S_{QPD} shall have units of $m/Volt$.

Once calibration is set, the measurement of the position of the incident laser beam in two dimensions can be achieved for particle position determination [80, 81]. Moreover, the average intensity signal, representative of the total intensity of light that strikes onto the detector, has information related with the axial displacement of a trapped particle [23].

Additionally, if necessary, the optical power onto the detector can be calculated. With the transimpedance gain of $10kV/A$, the conversion of voltage to the photocurrent detected can be determined. Then, with the PDQ80A responsivity graph (Figure A.5 in

Appendix A section A.1), the conversion from detected photocurrent to optical power units can be computed [78].

3.2.2 Experimental protocol for sample preparation

For performing the experimental measurements presented in the subsequent chapters, and in order to ensure reproducible results, we establish an experimental protocol that was followed in the preparation of a set of reference particles. The experimental protocol depends on the type of measurement as will be described bellow.

The implementation of the protocol requires a set of materials: an eppendorf, two different micro-pipettes 1-10 μL (P10 model, GILSON) and 200-1000 μL (P1000 model, GILSON), the respective pipette tips (adapted to each micro-pipette), a glass beaker and a plastic pipette. The characteristics of the reference particles used for sample preparation (Phosphorex Inc., United States of America) are presented in Table 3.2.

Firstly, the solution contents must be homogenized to disperse the particles. Then, the glass beaker is used to store the medium, which can be either deionized water or NaCl solution. After that, the eppendorf is placed in a support and the micro-pipettes with the respective pipette tips are used to take the desired volume from the particle contents and from the selected solvent. Then, to homogenize the prepared solution the eppendorf is turned up and down. Lastly, the plastic pipette is used to place a fraction of the prepared sample in the coverslip surface of the sample holder. A volume of approximately 80 μL is used for each measurement.

TABLE 3.2: Materials and optical characteristics of the particles used in the experimental measurements (from Phosphorex Inc., United States of America).

Particle type	**Particle dimensions**	**Refractive Index (@976 nm)**
PS microspheres	3 μm, 4 μm, 8 μm	1.5731 [83]
PMMA microspheres	3 μm, 8 μm	1.4824 [83]
Yeast cells	7 μm	
Chlorella Vulgaris	3-5 μm	

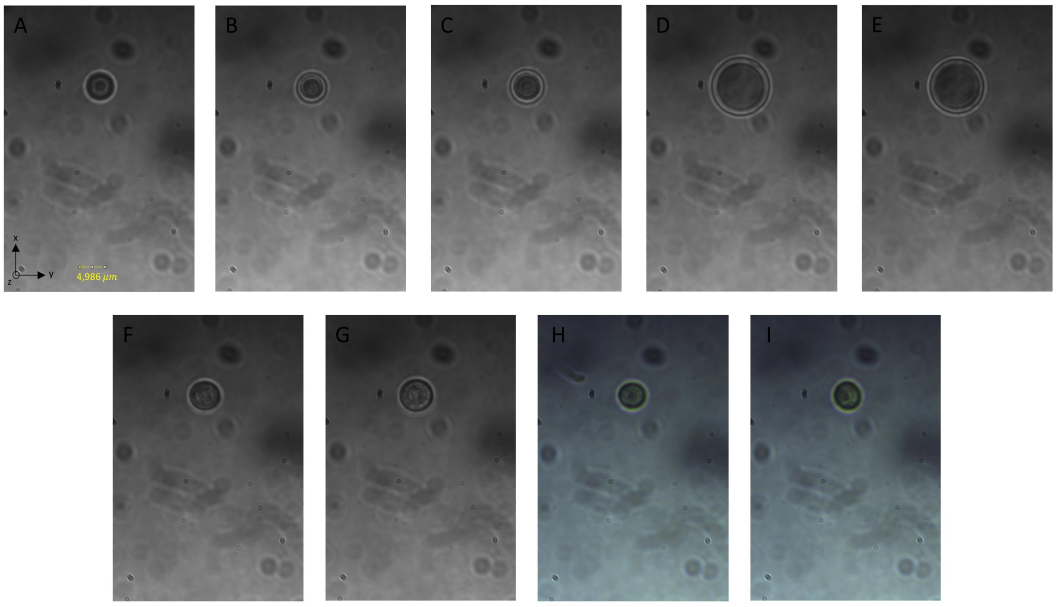

FIGURE 3.7: Images acquired in Thorcam software (Thorlabs) that represent the different particles and cells used to measure the optical forces and to test the classification capabilities of the system. In segment A, the Cartesian axis is presented along with the displacement conversion factor, measured in ImageJ software, based on the pixel size and image magnification. A- 3 μm PMMA microspheres; B- 3 μm PS microspheres; C- 4 μm PS microspheres; D- 8 μm PMMA microspheres; E- 8 μm PS microspheres; F,G- 7 μm yeast cells; H,I- 5 μm Chlorella Vulgaris microalgae.

To perform calibration procedures, namely the lateral position calibration and the axial position calibration, the particles under study need to be fixed to the substrate, for the detection of the beam position as a function of the displacement of the particle. For that, a 0.05% Polystyrene (PS) solution was prepared by diluting 1 μL of a PS stock solution in 2 mL of 1 M NaCl aqueous solution. The obtained mixtures, containing microparticles ranging from 1 μm to 3 μm, were used for calibrations purposes. In these solutions, the beads Brownian motion decreases till they get fixed to the surface of the coverslip. This is due to the ionic nature of the NaCl solution that shields the intrinsic surface charge of the microspheres [76]. To ensure the particles are fixed to the substrate, the solution should be left to set for 30 minutes. Subsequently, when the laser is turned on the fixed particles should not move.

To conduct the optical force measurements and to test the classification capabilities of the system, a 0.05% PS and PMMA solution was prepared by diluting 1 μL of the stock solutions in 2 mL of the aqueous solution (deionized water, n=1.3270 @976 nm [84]). Furthermore, other testing solutions were prepared, namely a 10% Chlorella Vulgaris microalgae solution, and a diluted commercial yeast cells solution. The size of the particles and cells chosen varies from 3 μm to 8 μm. The images relative to the different particle

types and dimensions, acquired by the CMOS camera with the Thorcam software (Thorlabs), are presented in Figure 3.7.

3.2.2.1 Sample Holder

In the first experiments, the sample solution was loaded into a microscope slide with a built-in channel (ibidi), as can be seen in Figure 3.8A. The channel height of the microscope slide is 0.2 mm and the volume approximately 50 μL, which is optimal for optical tweezers experiments. However, after several attempts, we concluded that this step was not reproducible, due to the careful handling necessary to load the sample into the channel, along with the time necessary to properly clean it. In addition, the channel was accumulating a set of particles and so a new approach became essential.

In order to successfully perform the optical trapping it is required that the focal point of the laser beam is located at the same depth of the sampled particle. In this context, the high focusing power of the objective, and correspondingly short depth of field, results in a very short working distance of 0.23 mm. This means that in practice, for successful trapping to be attained, we should work with a very thin glass window, that allows working at such short distances.

Considering these limitations, and the geometry of the holders, the customised support shown in Figure 3.8B was designed and produced with a 3D printer. The structure produced has a free space to place a coverslip of 0.02 mm of thickness, which allows to load the sample on its surface while enabling the trapping in the sample plane.

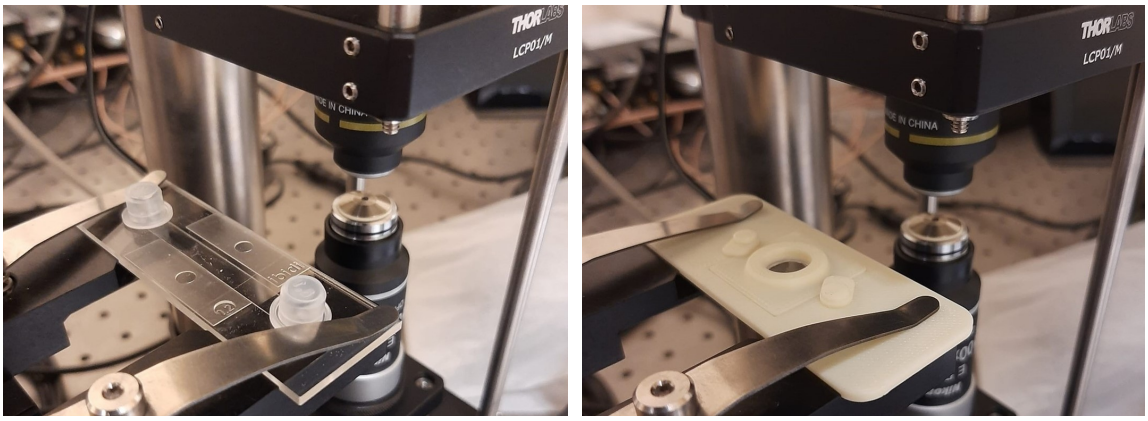

(A) (B)

FIGURE 3.8: Structures available to load the sample. (A) Figure illustrating the microscopy slide with built-in channel (from ibidi) placed in the slide holder in the modular optical tweezers system. (B) Figure illustrating the structured produced in the 3D printer placed in the slide holder in the modular optical tweezers system.

3.3 Closing remarks

In this chapter, we described the experimental setup and discussed some of the important concepts of the assembly and operation processes. The principles of the back focal plane detection were also addressed to characterize the operation of the quadrant photodetector used for calibration and functionalization purposes. To finalize, we have also detailed the protocol used in the experimental measurements of this project and that are presented in the subsequent chapters.

Chapter 4

Experimental measurements of optical trapping forces

After an overview of the working concepts of optical tweezers and a description of our experimental setup, this chapter focus on the experimental measurements conducted for its characterization and calibration. Initially, the study of the Gaussian beam propagation is presented, namely the investigation on the laser beam symmetry and the corresponding divergence and spot size, which is essential for the characterization of the system. To this follows the calibration of the quadrant photodetector, presented by means of the lateral position calibration and axial position calibration. The stiffness of the optical trap is then determined through two passive methods, the Equipartition method and the Power Spectral Density method, characterizing the optical trapping forces that are compared against the Boltzmann statistics method.

4.1 Characterization of the optical tweezers system

A complete characterization of our system requires the determination of several parameters. One of the most important is the behaviour of the laser beam on the detector, in particular the spot size of the laser beam in the transverse directions, as well as the divergence of the trapping laser. Additionally, the detector calibration factor is also crucial for an accurate study of the optical forces involved. In this section, we present a theoretical description of the calibration methods along with the experimental results and a brief discussion.

4.1.1 Measuring the beam shape

As the working principle underlying optical tweezers setups relies on the laser source properties, the measurement of the shape and size of the trapping laser near the focus of the lens is a crucial task for the characterization of the system's performance. To do so, we make use of the knife-edge method, one of the most common techniques used to determine the spot size of a Gaussian beam. This method displaces a sharp edge perpendicularly to the laser beam axis, detecting the changes of the total transmitted intensity as a function of the knife-edge position [85, 86]. A visual description of the standard knife-edge technique can be observed in Figure 4.1A.

As our optical tweezers system does not feature a standard detector, we adapted the technique by performing the standard knife-edge technique with the quadrant photodetector. Additionally, due to the fact that the working distance of the microscope objective is extremely small, the sharp edge object was replaced by a single mode optical fiber (SMF-28, Thorlabs) with the plastic coating, as seen in Figure 4.1B. Indeed, for such small working distance, the use of the sharp object, would either cause the obstacle to be positioned away from the minimum beam waist, or it could damage the microscope objective.

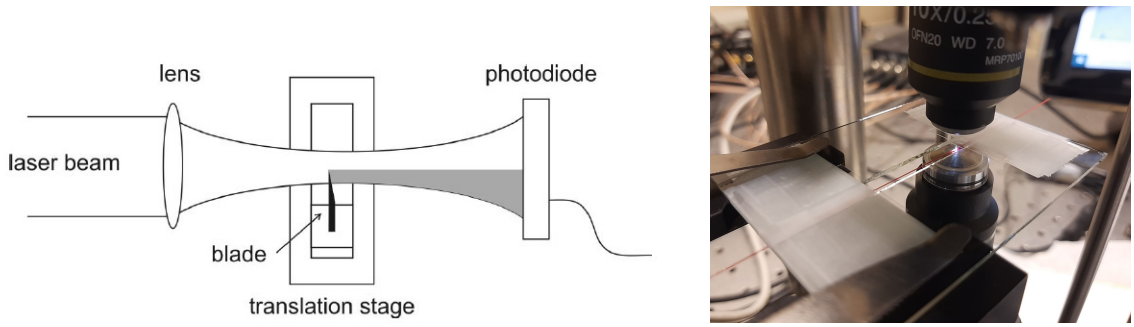

(A) (B)

FIGURE 4.1: Knife-edge technique used to determine the beam waist. (A) Representation of the knife-edge technique with a blade and a standard photodetector [85]. (B) Representation of the adapted knife-edge technique with a single mode optical fiber and a quadrant photodetector in a conventional optical tweezers system.

As referred previously, the quadrant photodetector returns three signals, the $XDiff$ normalized signal, the $YDiff$ normalized signal and the SUM signal. The SUM signal could be used to detect the total transmitted power as a function of the knife-edge position. However, in OTKB Software the recorded signals correspond to the displacement in x direction and y direction, and it only records the respective $XDiff$ normalized and $YDiff$ normalized signals.

The knife-edge technique was then adapted by recording the displacement in x and y direction along with the respective normalized signals. The displacement was controlled by the piezo controllers in closed loop operation mode (for more specifications related to closed loop operation mode consult section B.2 from Appendix B). Contrary to a standard photodetector method, the difference normalized signals are minimum when the entire beam hits the detector, as these signals are related to the position of the laser beam relatively to the center of the photodiode array, as reported in section 3.2.1. Furthermore, note that using the quadrant detector means that depending on the scan direction, the X and Y signals can increase or decrease with the displacement. If the scan is performed in the horizontal direction, in the "positive way" the X signal increases. Alternatively, if in the "negative way", the X signal will decrease. Yet, the difference is just the positive or negative shape of the signal, and the relevant shape of the curve obtained by either method is preserved.

The scan was performed both in the x and y direction to evaluate any elliptical behaviour. To measure the beam divergence, the same methodology was implemented varying the axial position instead (z direction) and recording the X and Y signals with the displacement of the positioning stage. For this purpose, the APT and the OTKB Software were employed in closed loop operation mode. The scans were performed as close as possible to the objective lens, and for the determination of the spot size, the position $z \approx 0$ was associated to the minimum distance tested.

The data treatment was implemented in *Jupyter Notebook*, where a Python script was built to perform the calculations. The standard *numpy* library was used along with the *scipy.optimize* library, namely the *curve_fit* function. The spot size of the laser beam was determined through the derivative of the X or Y signal, dependent on the knife-edge position that is in turn related to the displacement of the piezo controllers. After the computation of the derivative, the *curve_fit* function was used to find the optimal parameters of a Gaussian curve.

4.1.1.1 Experimental results

Figure 4.2 presents an illustration of the resulting data from the knife-edge process and of the computational procedure for the determination of the spot size. It can be seen that the axis scan was performed in the "negative way" of the y axis, which corresponds to a decrease of the Y signal acquired (represented by the blue color), as depicted in Figure

4.2A. With the variation of the recorded signal, the corresponding derivative can be obtained (represented by the red color) and consequently the Gaussian fit can be computed (represented by the black color). Following that, the FWHM and the spot size of the laser beam was determined as depicted in Figure 4.2B.

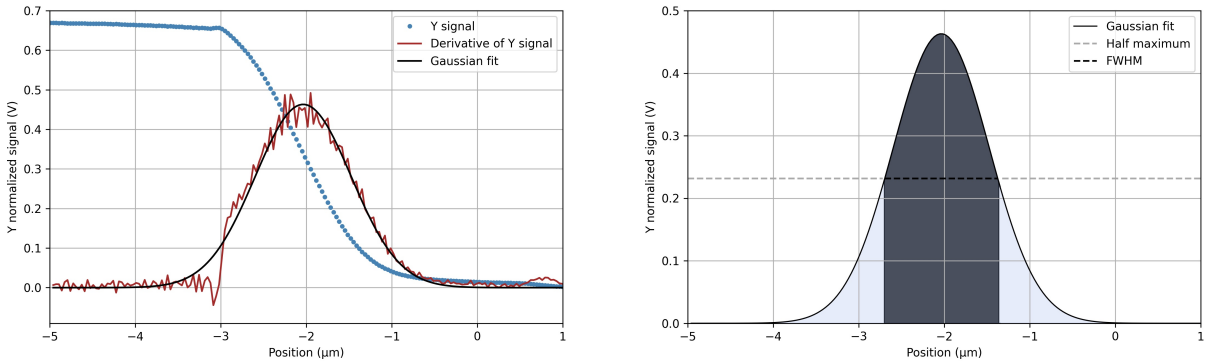

(A) (B)

FIGURE 4.2: Implementation of the knife-edge method to determine the spot size of the laser beam for 9.870 mW of optical power in the sample plane. (A) From the recorded Y signal (represented by the blue color) its derivative can be found (represented by red color) and the Gaussian fit can be computed (represented by black color). (B) Representation of the FWHM for the determination of the spot size.

The beam waist of the laser beam was determined both for the x direction (X-scan) and y direction (Y-scan). The results obtained are depicted in Table 4.1. Ideally, for the intended setup, the spot size of the laser beam should be symmetrical, meaning that the spot size determined should be the same for both directions. Nevertheless, an elliptical or asymmetrical shape can be observed due to the nature of the laser beam, the aberrations of the optical components, and the insufficient length of the single mode optical fiber (SM 980-5.8-125, Thorlabs), which acts as a spatial filter.

The experimental results depicted in Table 4.1, show that the values presented for the Y-scan, are indeed lower in comparison to the values presented for the X-scan, which shows a tendency towards an elliptical spot size shape. In particular, for lower optical powers, the percentage difference between the scans is higher, especially for 9.870 mW, where the difference is nearly 40.1 %. Additionally, for the X-scan the spot size decreases with the increase of intensity of the laser beam which corresponds to the expected behavior which, however, is not verified for the Y-scan.

TABLE 4.1: Determination of the beam waist through the knife-edge method, for four different optical powers in the sample plane.

Optical power (mW)	**X-scan (μm)**	**Y-scan (μm)**
9.870 mW	1.97 ± 0.03	1.30 ± 0.05
22.575 mW	1.80 ± 0.03	1.38 ± 0.02
35.070 mW	1.52 ± 0.52	1.38 ± 0.04
47.070 mW	1.43 ± 0.02	1.43 ± 0.07

The knife-edge method was also employed for the study of the beam divergence. The same methodology was implemented varying the different axial displacements instead. The piezo controller, responsible for the axial displacement, was set to four different positions, corresponding to the displacements presented in Table 4.2, as measured by the strain gauger reader, and corresponding to a driving PZT voltage of $10V$, $30V$, $50V$ and $75V$, respectively. In this experiment, the optical power used was 9.780 mW and only one measurement for each axial displacement was recorded. The laser beam propagation was studied for several axial displacements. With the increase of the axial position, the growth of the spot size is verified, as expected, apart from a few exceptions that may arise from experimental fluctuations.

TABLE 4.2: Experimental results obtained with the knife-edge method, for 9.870 mW considering four different axial displacements.

Axial displacement (μm)	**X-scan (μm)**	**Y-scan (μm)**
2.026 ± 0.008	2.54 ± 0.02	1.54 ± 0.02
7.135 ± 0.008	2.91 ± 0.02	1.44 ± 0.02
12.827 ± 0.003	3.65 ± 0.02	2.11 ± 0.02
20.247 ± 0.004	3.55 ± 0.02	2.81 ± 0.02

Although we can not ensure that the beam waist was exactly determined in the focal spot (in Table 4.1), the comparison of the signals recorded for each axial position is still valid. In Figure 4.3 the corresponding Gaussian fits resultant of the derivative of the signals recorded for the Y-scan, are presented. The shape of the signal highly determines the size of the spot obtained for each axial displacement, as observed. Additionally, as depicted above, at axial positions away from the focal plane, the spot size increases. This is verified for all the axial displacements with the exception of displacement at 2.026 μm

and 7.135 μm, for the scan in the y direction, as depicted in Table 4.2. This uncertain measurement can be clearly observed in between the green curve (Gaussian fit at 10 V) and the orange curve (Gaussian fit at 30 V).

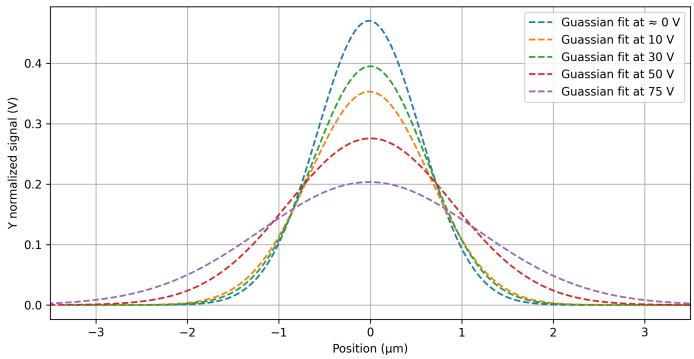

FIGURE 4.3: Representation of the Gaussian fit function for Y-scan for each axial position to determine the spot size of the laser beam, for 9.870 mW, for several axial displacements.

By observing the results, we verify that for the position closer to the objective lens, the average spot size along the x and y directions were 1.97 μm and 1.30 μm, respectively. The values obtained are quite close to the expected diffraction limit presented in section 2.2, indicating that we are located near the focus region. Additionally, the measurements conducted with the knife-edge method were performed without the immersion oil, and if the objective lens is used without the immersion oil the corresponding numerical aperture will be smaller and the spot size will increase accordingly. Also, we concluded that the beam profile deviates from the expected symmetrical cross-section, and this must be analysed in the future.

Furthermore, we remark that the position observed in the y-axis is related to the displacement of the positioning stage in the y direction, and not with the axial displacement.

4.1.2 Lateral position calibration

A complete characterization of the quadrant photodetector requires two major calibrations, the lateral position calibration and the axial position calibration. The lateral position calibration, as the name suggests, is performed transversely to the laser beam propagation. In this calibration, the changes in X and Y signals associated to the signal emerging from a stuck bead are analyzed along with the corresponding displacement [4, 77]. In the axial position calibration, the stuck particle is displaced along the direction

of the laser beam optical axis. The total transmitted power (SUM signal) is recorded for several known axial positions of the bead (z direction) [4, 86].

One of the most common methods to perform the lateral position calibration is the stuck bead method. Basically, a particle is fixed to the surface of a coverslip and then displaced along the laser spot, recording the signals in the x and y direction. The stuck bead method requires several steps. First, a target is placed in the computer screen, to mark the area that corresponds to the near infrared laser spot. Then, histogram lines are set in the horizontal and vertical direction to intersect the point were the center of the beam is located. Following, as described in section 3.2.2, the solutions prepared for the calibration procedures are loaded into the sample holder. For calibration purposes, the dimension of the fixed bead is important to be around the same order of magnitude as the laser spot size, to accomplish good results. Indeed, on account of light diffraction, ring patterns generated for particles of bigger dimensions creates differences of intensity that make the calibration process more difficult.

The displacement of a fixed bead along the optical trap creates a change in the signal, which can be used to compute the detector responsivity factor by means of the slope of the acquired signal. In Figure 4.4 we present a schematic of the calibration process and typical results for the change of the recorded V_x output signal with the horizontal displacement of the particle. In scheme A, the laser beam reaches the detector without crossing any obstacle and a constant V_x signal is acquired. In scheme B, the fixed particle crosses the left side quadrants and the intensity signal that strikes the detector on the positive side decreases, which decreases V_x. In scheme C, the particle is centered with the laser spot and the beam is deflected evenly in all quadrants. In scheme D, the beam intensity is greater in the positive side than in the negative side and so the V_x signal remains positive before decreasing to approximately zero again. Thus the voltage data obtained with the quadrant photodetector can be converted to units of displacement, by the analysis of the slope of the lateral position calibration curve.

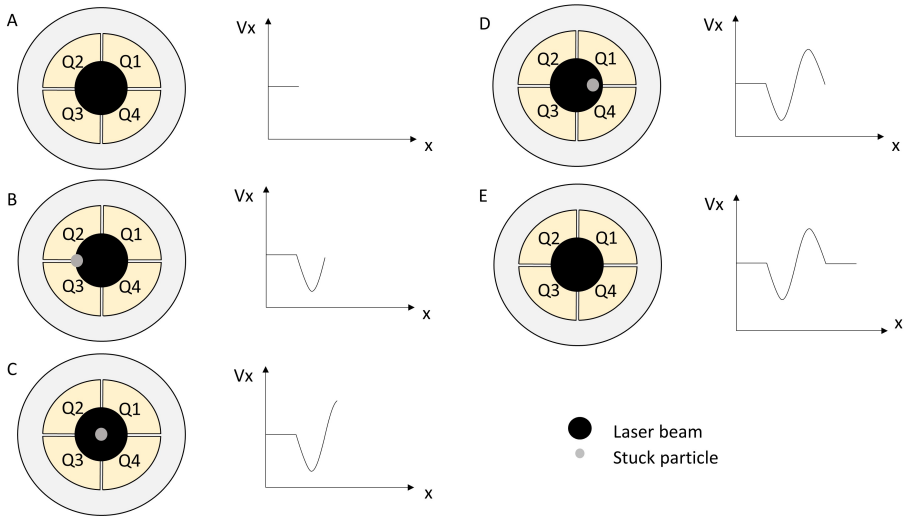

FIGURE 4.4: Schematic of the stuck bead method employed for lateral position calibration. The fixed bead is displaced across the laser spot and the V_x signal is recorded. The circle colored in black is representative of the laser beam onto the detector. The circle colored in gray is representative of the particle fixed to the coverslip, placed in the sample plane, which is displaced in the x direction.

Before advancing to the results, we must note that the conversion factor is valid only for the region of linear response of the detector which, accordingly to the literature [4], is valid up to a recommended maximum displacement of three micrometers. This recommended limit is within the displacement range observed for the trapped particles. Additionally, the lateral position calibration must be repeated for a range of laser powers, as the trapping and detection laser are the same. In fact, different powers can affect the dimension of the trapping spot and the deflection of the beam onto the detector can vary.

4.1.2.1 Experimental results

For the experimental measurements, the system was properly set to close loop operation mode, and the displacement in the traversal directions was recorded along with the corresponding normalized signals, X signal and Y signal. The experimental measurements were conducted with NaCl solutions of 0.05% Polystyrene (PS) microparticles of 1 μm size (sample preparation is described in section 3.2.2). The differential signals were adjusted to minimum ($\approx 0V$) to ensure the laser was properly centered onto the detector.

In Figure 4.5A and Figure 4.5B the lateral position calibration for both transverse directions is presented. It is straightforward to observe the predicted intensity variation which results from the deflection of the laser beam onto the detector as detailed before.

For each optical power, six signals were recorded and the corresponding mean value was computed to determine the detector responsivity factor ($V/\mu m$) of the *S-curve*. The detector responsivity can be inverted and converted into a conversion factor (m/V), which is presented in Table 4.3.

TABLE 4.3: Lateral position calibration for the determination of the conversion factor for four different optical powers in the sample plane.

Optical power (mW)	**Conversion factor X-Scan (m/V)**	**Conversion factor Y-Scan (m/V)**
9.870 mW	$(1.28 \pm 0.08) \times 10^{-6}$	$(1.53 \pm 0.07) \times 10^{-6}$
22.575 mW	$(1.25 \pm 0.07) \times 10^{-6}$	$(1.25 \pm 0.04) \times 10^{-6}$
35.070 mW	$(1.22 \pm 0.06) \times 10^{-6}$	$(1.7 \pm 0.1) \times 10^{-6}$
47.502 mW	$(1.3 \pm 0.1) \times 10^{-6}$	$(1.7 \pm 0.1) \times 10^{-6}$

From the analysis of the table it can be observed the existence of slight difference between the X-Scan and the Y-Scan, which can be resultant of multiple factors. A first explanation, related with the shape of the signal, can be the beam asymmetry as suggested in the beam spot measurements. Also, it is possible that some misalignment along the optical path can be present, in particular, axial misalignment can be detected by the uneven illumination of the sample plane, which can cause differences of intensity. The camera itself might not be fully aligned with the horizontal and vertical directions of the respective piezo controllers. Additionally, the laser beam might not be exactly positioned in the center of the photodetector array, as well as the positioning of the target in the computer screen, which could be displaced from the real trap position. Finally, the particle itself can introduce some of the difference observed between the scans, as it might not be completely spherical. All these factors are hypothetical explanations for the difference obtained, and should be addressed carefully in future studies which due to the constrained schedule, were left outside the scope of the dissertation.

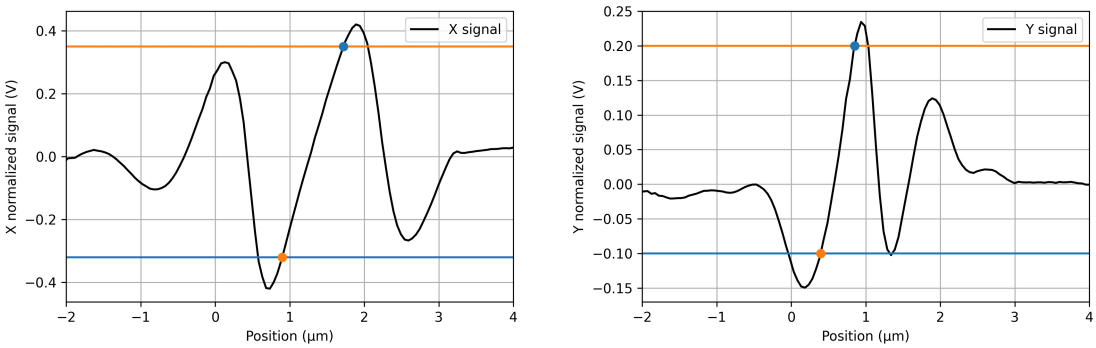

(A) (B)

FIGURE 4.5: Lateral position calibration based on the scan of a fixed bead across the spot size, for an optical power of 47.502 mW in the sample plane. The horizontal lines allow the determination of the slope between the two intersection points (colored in blue and orange). (A) Representation of the scan in the x direction. (B) Representation of the scan in the y direction.

Despite being widely used, the method employed for the position calibration has some disadvantages that we must discuss. One of the major disadvantages is the fact that the positioning of the bead in the exact location of the spot size is a difficult process. Indeed, we can not guarantee that the calibration is performed in the exact region where the experimental measurements are conducted, for instance for optical force determination as presented later on in this chapter. Also, the behaviour of a trapped bead can be highly affected by the proximity with the coverslip, and thus the calibration near the surface is not that intuitive [87]. In addition, if the regime of small displacements is still verified for trapped particles of bigger dimensions, the calibration factor obtained for particles of small dimensions remains valid.

Furthermore, a possible validation process of the calibration methodology is to seek alternative reference calibration methodologies, such as the that of inference from the Brownian motion of a trapped particle [27]; this method, is of particular usability for systems that do not have piezo positioning.

4.1.3 Axial position calibration

For the axial position calibration we adapted the method, recording the total transmitted power instead (SUM signal) for several axial positions (z direction), introduced manually in the APT Software. After that, for each axial displacement, the mean value of the SUM signal was determined.

In practice, the axial position calibration is harder to implement due to the refractive index mismatch that exists between the particles and the surrounding medium, which can cause focal shift or even spherical aberrations [4].

4.1.3.1 Experimental results

The experimental measurements were conducted with NaCl solutions of 0.05% Polystyrene microparticles of 3 μm size (sample preparation is described in section 3.2.2). The measurements were executed for three different optical powers. In Figure 4.6A, it is presented the total transmitted power as a function of the axial displacement. In this calibration procedure, for each optical power, the bead was first positioned below the focus ($-z$). Following that, the particle was displaced to the $\approx$ 7-8 μm position, corresponding to the approximate location of the focal plane ($z \approx 0$). Finally, the bead was displaced to a site above the focus ($+z$).

Observing the increase of the transmitted signal onto the detector, we can immediately relate it to the increment of the optical power used. As presented, for each optical power, the signal increment in the region above the focal plane ($+z$), is related to the focusing effect of the particle which acts as a lens, as it converges the beam onto the detector. On the other hand, when the bead is located below the focus ($-z$), the laser beam diverges and the intensity decreases. The increase and decrease of signal verified can thus be related to the refractive index mismatch between the fixed particle and the surrounding medium. The experimental results are in accordance with the literature results [86] and the described behavior as it can be observed in Figure 4.6.

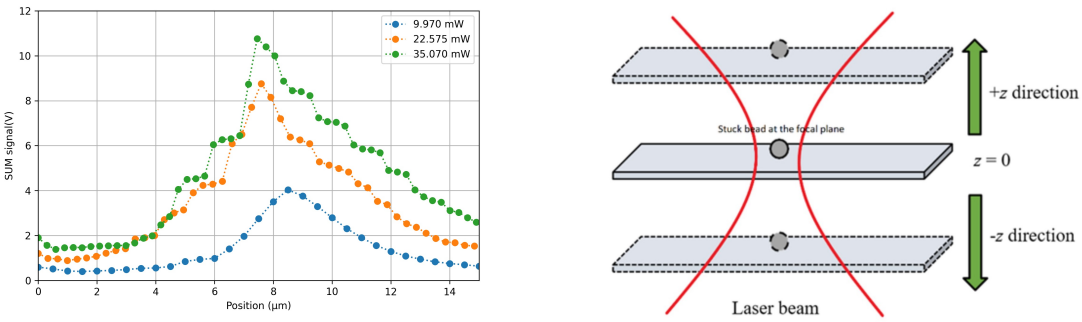

(A) (B)

FIGURE 4.6: Representation of the axial position calibration (A) The transmitted signal along the axial displacement, for three different optical powers. (B) Position of the fixed particle relative to the origin ($z = 0$), which is the focal plane. The position located above the focal plane is designated as $+z$, and the position below as $-z$ [86].

4.2 Measurement of optical trapping forces

The trapping process is characterized by a distinct signature on the signal collected as depicted in Figure 4.7, which presents three different stages. The first stage, illustrated by the red color, represents the time at which the laser beam is turned off. Then, when the laser beam is turned on, the transmitted signal increases, represented by the green color. An abrupt intensity difference is then observed with a decrease of the detected signal, now represented by the blue color. This abrupt variation, here close to the 25 seconds time, expresses the time at which the particle was trapped. The decrease of the transmitted signal when the particle is trapped is related with the fact that the bead is not completely transparent to the radiation, absorbing part of it. Furthermore, it also scatters the beam out of the detector path.

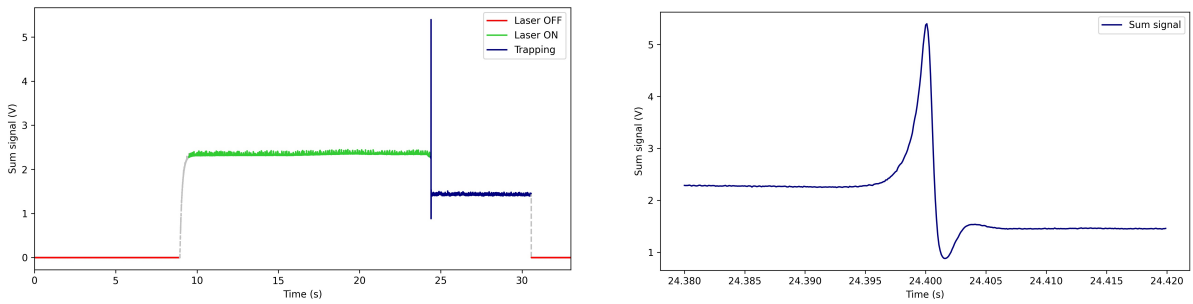

(A) (B)

FIGURE 4.7: Signal collected during the optical trapping of a 3 μm PMMA microsphere. (A) Three different levels are detected- when the laser is turned off (represented by the red color) -when the laser is turned on (represented by the green color) -when the optical trapping occurs (represented by the black color). (B) Optical trapping of a 3 μm PMMA microsphere.

Characterizing this trapped regime is a crucial step for a proper quantitative analysis and interpretation of the results. This requires the determination of the stiffness and the optical force acting on each trapped particle. To conduct the stiffness measurements, we prepared aqueous solutions (deionized water, n=1.3270 @976 nm [84]) of 0.05% Polystyrene and PMMA microparticles with sizes ranging from 3 μm to 8 μm, (sample preparation is described in section 3.2.2). For each type of sample, we acquired six distinct signals of 120 seconds of total duration at an acquisition rate of 10 kHz, and in open loop operation mode (for more specifications related to open loop operation mode consult section B.1 from Appendix B).

For the purpose of increasing the amount of data to determine the stiffness with a convenient statistical sampling, each 120 seconds acquired signal was divided in individual segments of 500 milliseconds forming the total dataset to be analysed. Following that, the stiffness was computed for each individual segment and the mean value of all segments was determined. The stiffness constant was determined using the Equipartition method and the Power Spectral Density method.

Additionally, we remark that the 500 milliseconds segment was strategic for the classification of data presented in the next chapter, and we decided to maintain the same conditions for data analysis and treatment.

4.2.1 Equipartition method

To determine the stiffness through the Equipartition method, we computed the statistical variance of the particle position for each 500 milliseconds segment. These fluctuations, resulting from the change of position of the trapped particle, are proportional to $k_B T$ constant and can be used for the determination of the stiffness constant as given in equation 2.15.

In Figure 4.8, we present the typical result obtained for the case of a 3 μm PMMA microparticle which are used to employ the prescribed methodology. The averaged results obtained for the stiffness constant through the Equipartition method, are presented in Table 4.4. The conversion factors used to compute the stiffness in SI (International System of Units) units are depicted in Table 4.3.

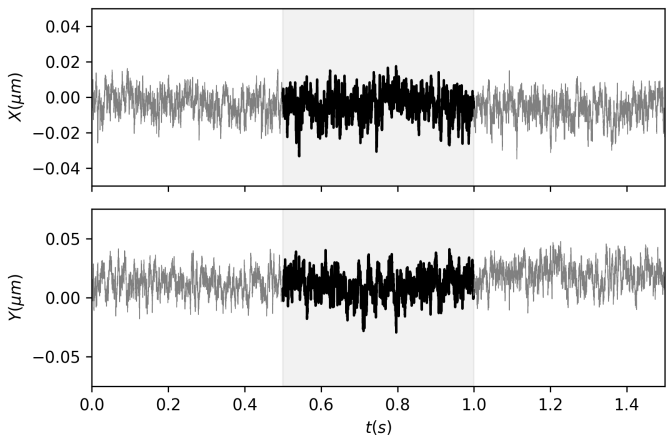

FIGURE 4.8: Stiffness constant determination for 3 μm PMMA particle through the Equipartition method, for 22.575 mW. The 500 millisecond segment is highlighted.

TABLE 4.4: Stiffness determination through the Equipartition method, for 22.575 mW. The experimental uncertainty was estimated here using the standard error of the mean.

Particle type	**Particle size(μm)**	**StiffnessX(N/m)**	**StiffnessY(N/m)**
Polystyrene microspheres	3 μm	$(1.01 \pm 0.04) \times 10^{-6}$	$(2.80 \pm 0.03) \times 10^{-5}$
	4 μm	$(1.9 \pm 0.1) \times 10^{-4}$	$(1.65 \pm 0.07) \times 10^{-4}$
	8 μm	$(5.19 \pm 0.06) \times 10^{-4}$	$(1.03 \pm 0.02) \times 10^{-3}$
PMMA microspheres	3 μm	$(1.39 \pm 0.03) \times 10^{-4}$	$(2.87 \pm 0.07) \times 10^{-4}$
	8 μm	$(2.73 \pm 0.05) \times 10^{-3}$	$(1.15 \pm 0.03) \times 10^{-3}$

The stiffness constant mainly depends on three experimental parameters, the laser intensity, the particle dimension and the corresponding refractive index. At thermal equilibrium, the particle fluctuations are generally larger for smaller particles in comparison to bigger size particles. Moreover, as the particle dimension decreases, the scattering component becomes more dominant and the optical trap gets less stiff.

Given the results obtained and presented in Table 4.4, we can see that the stiffness constant for x and y direction are quite similar, except for one case which may arise from experimental errors. Additionally, we can observe that for particles of higher dimensions, namely the 8 μm PMMA and the 8 μm Polystyrene microparticles, the stiffness constant is higher in comparison to smaller particles, which is in accordance with what was described above. When attempting to compare particles of the same size, particularly for the 3 μm and the 8 μm particles, in general the stiffness is higher for the PMMA microspheres in comparison to the Polystyrene microspheres.

To get an idea of the typical energy and force scales involved for the determined stiffness constants, we can plot both the predicted potential as well as the gradient optical force. As observed in Figure 4.9, the values of the potential energy are around a few $k_B T$ which, beating the thermal energy, allows to effectively trap the particle as discussed before. Using the stiffness value, it is also possible to determine the optical force, which is computed through equation 2.1. As it can be seen, it depends on the position of the particle in the optical trap relatively to the equilibrium position, and changes over time with values in the range of the picoNewton. This is in accordance with what is presented in the literature [4, 34].

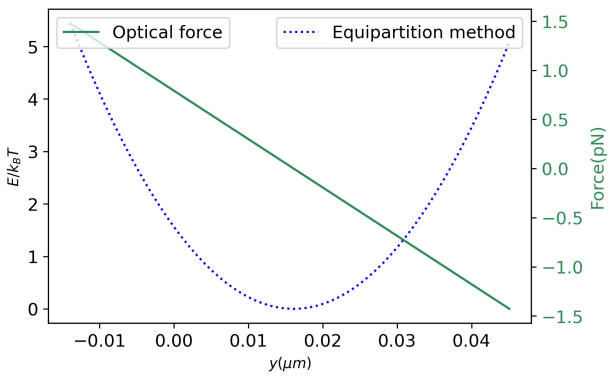

FIGURE 4.9: Potential analysis corresponding to an optically trapped 3 μm PMMA particle and the optical force, for 22.575 mW.

4.2.2 Power spectral density method

As seen in section 2.3.3 another method used to assess the stiffness constant is the Power Spectral Density method. Using the same data as in the previous section, we employed the standard *scipy* library and the *signal.welch* function to the time data domain (position fluctuations segments) to estimate the Power Spectral Density. After that, by fitting the one-sided power spectrum to a Lorentzian function, the corner frequency and the drag coefficient were extracted. Succeeding in gathering those constants, equation 2.17 was used for the determination of the stiffness constant.

In Figure 4.10, it is represented the Power Spectral Density and the corresponding Lorentzian fit for a 3 μm PMMA microparticle. The results obtained for the stiffness constant through the Power Spectral Density method, are presented in Table 4.5.

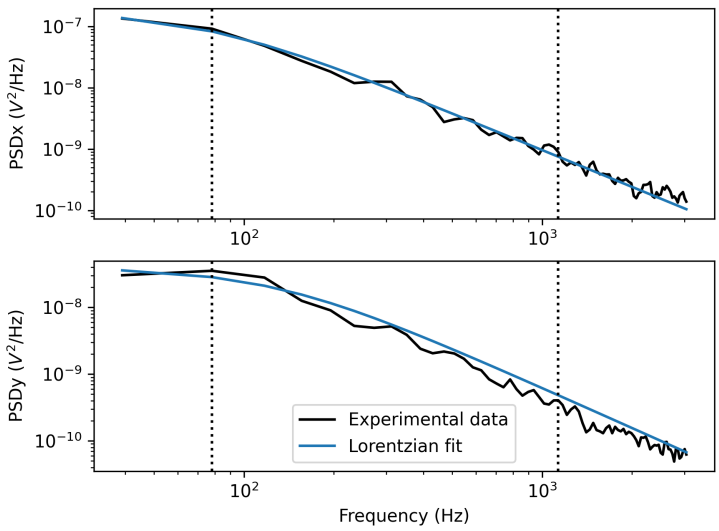

FIGURE 4.10: Stiffness constant determination for 3 μm PMMA particle through the Power Spectral Density method, for 22.575 mW.

TABLE 4.5: Stiffness determination through the Power Spectral Density method, for 22.575 mW. Again, the experimental uncertainty presented was estimated using the standard error of the mean.

Particle type	**Particle size**	**StiffnessX(N/m)**	**StiffnessY(N/m)**
Polystyrene microspheres	3 μm	$(9.6 \pm 0.5) \times 10^{-6}$	$(1.6 \pm 0.02) \times 10^{-5}$
	4 μm	$(2.0 \pm 0.1) \times 10^{-5}$	$(1.11 \pm 0.04) \times 10^{-4}$
	8 μm	$(4.6 \pm 0.1) \times 10^{-4}$	$(1.01 \pm 0.02) \times 10^{-3}$
PMMA microspheres	3 μm	$(9.6 \pm 0.2) \times 10^{-5}$	$(1.61 \pm 0.04) \times 10^{-4}$
	8 μm	$(3.78 \pm 0.07) \times 10^{-5}$	$(1.51 \pm 0.05) \times 10^{-3}$

Comparing the results of the two methods, we can say that in general, the stiffness values determined with the EP method are generally higher than the values obtained with the PSD method. This difference may be the result of the fact that the PSD method involves the fitting of two parameters, the corner frequency (f_0) and the friction coefficient (γ). Indeed, the double fitting procedure can be associated with an higher uncertainty in comparison to the process of extracting a single parameter from signal analysis, as usually employed in the literature [77].

4.2.3 Optical potential analysis

After obtaining the results for both the equipartition and power spectral density methods, we can now use the Boltzmann statistics methodology to compare both methods and to infer if the potential is indeed of the harmonic type. For that we have computed the probability density function using a normalized histogram as outlined in section 2.3.4. By computing the probability density function $\rho(x)$, the potential energy can be determined, for both x and y direction, as depicted in Figure 4.11. As it can be easily seen in Figure 4.11A, higher values of the probability of the particle position occurs at values of deeper potential, as expected.

The stiffness computed through the EP method and PSD method can be used to reconstruct the corresponding optical potential and allow the comparison between themselves and that acquired with Boltzmann statistics. As depicted in Figure 4.11B, the behaviour of the potential energy function is quite similar for all the three methods, especially for the x direction. In particular, the trapping potential obtained from the PSD

method is slightly weaker in comparison to that obtained from the EP method and Boltzmann statistics, which have a similar behaviour.

As referred, an advantage of the method is that it can be used to evaluate if the potential is indeed of the harmonic type. Observing the comparison of subfigures B of Figure 4.11 with the results obtained for the equipartition method, we can easily conclude that the potential is indeed harmonic in the region of interest, which qualitatively validates the experimental setup.

This method can also be used to provide some visual hints on the trap shape and orientation relatively to the x and y axis. Together with the analysis depicted in section 4.1 it can be used to infer that the trap is probably not perfectly aligned with the system. Instead, the trap is rotated approximately 45° degrees, which can affect the detection, as the trap is not aligned with the axis of the photodiode array. Furthermore, note that this potential analysis can also be used for the determining the stiffness of trap using a standard curve fitting procedure. Again, due to schedule issues, these two notes were left out of the scope of the dissertation and should be explored in future investigations.

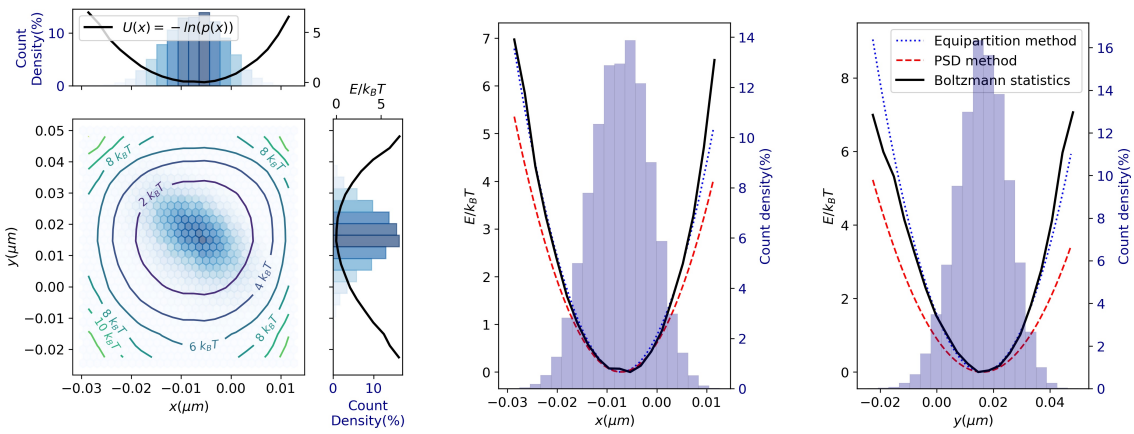

(A) (B)

FIGURE 4.11: Position histogram and optical potential for a 3 μm PMMA trapped particle, for 22.575 mW. (A) Position histogram for x and y direction. (B) Optical potential representation for Equipartition method, PSD method and Boltzmann statistics, for x and y direction.

4.2.4 3D trapping

Finally, to prove that the particle is indeed trapped in all the three dimensions, we have tested the response of the transmitted signal when the system is submitted to an

axial perturbation (in the $+z$ direction). For this, we used an aqueous solution (deionized water, n=1.3270 @976 nm [84]) of 0.05% Polystyrene (PS) microparticles of 3 μm size (sample preparation is described in section 3.2.2)

Different outcomes can result from an axial perturbation depending on the relative position of the particle to the coverslip and on its distance to the trap's axial centre. For a particle located below the focal plane near the equilibrium position, to an induced axial perturbation the bead remains near the equilibrium position and consequently the intensity of the transmitted signal does not change, as observed in Figure 4.12. Represented by the red arrows, the abrupt changes relate the perturbations created with the way the system responds to preserve the stability of the three dimensional optical trap.

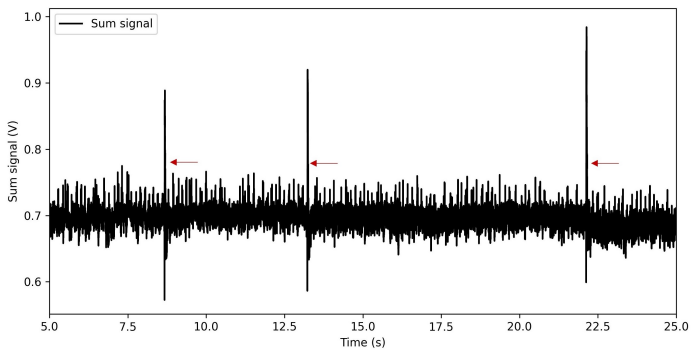

FIGURE 4.12: Optical transmission signal for 9.870 mW. The time when the axial perturbation was generated is represented by red arrows.

Oppositely, for a particle located above the focus, the trap was not able to pull the bead towards its center, as can be seen in Figure 4.13. In this case, only the transverse stability of the particle can be maintained, which reflects as an increase of the transmitted signal with the axial shifts, represented by black arrows. The scattering force dominates and the trap is not able to pull the particles towards the center. These variations indicate that the position of the particle is no longer in the focal plane but above it, as already discussed for Figure 4.6.

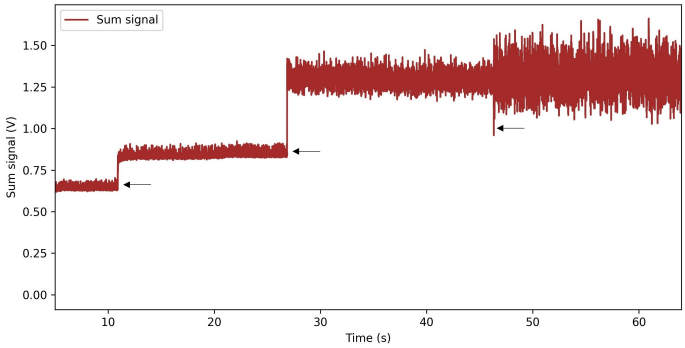

FIGURE 4.13: Optical transmission signal for 9.870 mW. The time when the axial perturbation was generated is represented by black arrows.

4.3 Closing remarks

This chapter reported the experimental procedures and results conducted over this project for the characterization and calibration of the optical tweezers systems. We discussed the characterization of the trapping beam by the determination of the spot size and the calibration of the quadrant photodetector, including both the lateral position calibration and the axial position calibration. After that, we employed the equipartition and power spectral density methods for determining the force observed for distinct particles. The behaviour of the trapping potential obtained for the distinct methods was also discussed. As predicted, distinct particles feature distinct behaviors when trapped by the optical beam. As such, analysing data related with this response can be useful for classifying the type of particle that is trapped, a feature that will be explored in the next chapter.

Chapter 5

Particles and cells classification by the analysis of the forward scattered signal

So far we introduced the working concepts and characterized the optical tweezers system that was assembled during the project. In this chapter, we present one possible application of the system, introducing the possibility to classify the trapped particles and cells based on the data acquired with the quadrant photodetector. First, we discuss the context of the problem and introduce the classification algorithms and the corresponding procedures. In particular, comparing with the literature, our solution presents a novel preprocessing procedure using principal component analysis (PCA) in the Fourier domain to perform the extraction of relevant features and the dimensionality reduction. These features are then used to train and test the classification algorithms chosen. In the second part of the chapter, we present the results for the classification task for different particle types, discussing the overall accuracy and potential to distinguish between different classes. Before closing the chapter, we provide a comparison between our system and an optical fiber-based solution, allowing to conclude that a conventional optical tweezers system can outperform the fiber solution for the classification task with the addition of the quadrant photodetector system.

5.1 Particle classification using the forward scattering signal

Light scattering-based techniques are currently one of the most common approaches for detection and characterization of small particles. Yet, while techniques like flow cytometry are well-established and capable of measuring the shape and size of particles and cells, they often offer average measures for a population and not work at an individual level. In this context, we can argue that deploying a classification tool with optical tweezers can be an important step for fields which require a higher degree of control, such is the case of personalized medicine for cell sorting.

In this section, we explore and implement a classification methodology for particles and cells with the signal acquired using a quadrant photodetector in our conventional optical tweezers system. The underlying concept is that the position fluctuations of the trapped particle are in principle connected with the properties of the particle through its dynamics and thus allow to identify a particle type through its temporal scattering signal. The classification procedure proposed in this work utilizes the 3-channel signal retrieved from the QPD (X, Y, SUM), to classify individual particles of different classes.

5.1.1 Experimental methods

To deploy the classification algorithm and test its capabilities, we acquired the signals from aqueous solutions (deionized water, n=1.3270 @976 nm [84]) of 0.05% PS and PMMA microparticles, of 10% Chlorella Vulgaris microalgae and the dilution of commercial yeast cells, with sizes ranging from 3 μm to 8 μm, (sample preparation is described in section 3.2.2). Additionally, aqueous solutions of 0.05% PS and PMMA with sizes ranging from 100 nm to 500 nm, were used for the nanoparticles case. For each bead type, we acquired 6 distinct signals of 120 seconds of total duration at an acquisition rate of 10 kHz.

In order to approximate the acquired data to a real-world scenario of fast classification, each acquired signal, with a total duration of 120 seconds acquired at an acquisition rate of 10 kHz, was divided into individual segments of 500 milliseconds, forming the total dataset. Then, for each signal and for each channel, the standard *numpy* library was implemented to compute the Fourier transform by means of the Fast Fourier Transform (FFT) algorithm. As the continuum component does not contain relevant information regarding the particle dynamics, we neglected it to avoid unnecessary noise in the classifier.

5.1.2 Pre-processing procedure

The principal component analysis is an algorithm commonly used for reducing data dimensionality, while maintaining most of the dataset characteristic variation. The reduction of the data space focuses on the identification of new variables, the principal components, which consist of linear combinations of the old variables, and correspond to the directions of the maximum data variation [88].

This unsupervised data analysis was implemented with the standard *sklearn* library, where a tendency along the frequency space was extracted, which enabled the description of the variation of the Fourier transform observed, for the total dataset. This algorithm, which acts in the co-variance space, was used to extract the two most relevant components of the PCA, for each channel signal, in the Fourier space. As an example, in Figure 5.1, it is illustrated a two-dimensional PCA plot with two principal components, which represent the extracted features, for the channel X. Furthermore, in addition to the projection in this space, we note that the principal component analysis is able to reduce the stochastic noise of data in the Fourier domain, which indicates the filter capacity of the PCA. Consequently, the relevant components in the frequency domain can be described as smooth lines, as it can be observed in Figure 5.2.

With this in mind, for a segment of dimension of 3 channels $\times$ 5000 data points, which equals to 15000 variables, the extraction of the relevant features, enabled the reduction to the 6 most relevant features of the co-variance space.

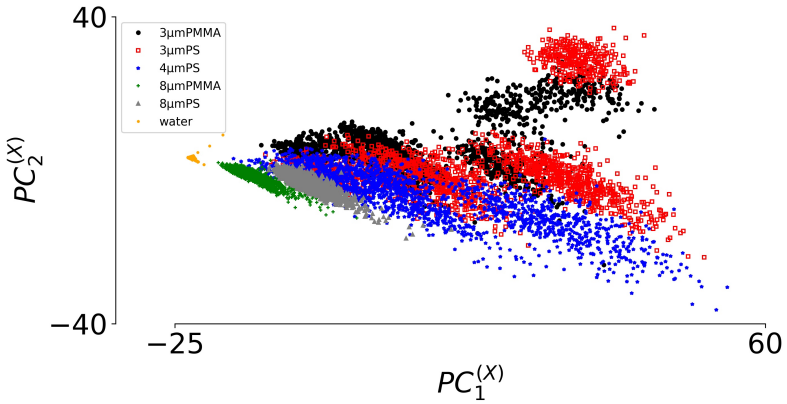

FIGURE 5.1: PCA plot of the corresponding Fourier transforms for the tested synthetic particles, depicting the two principal components of the X signal.

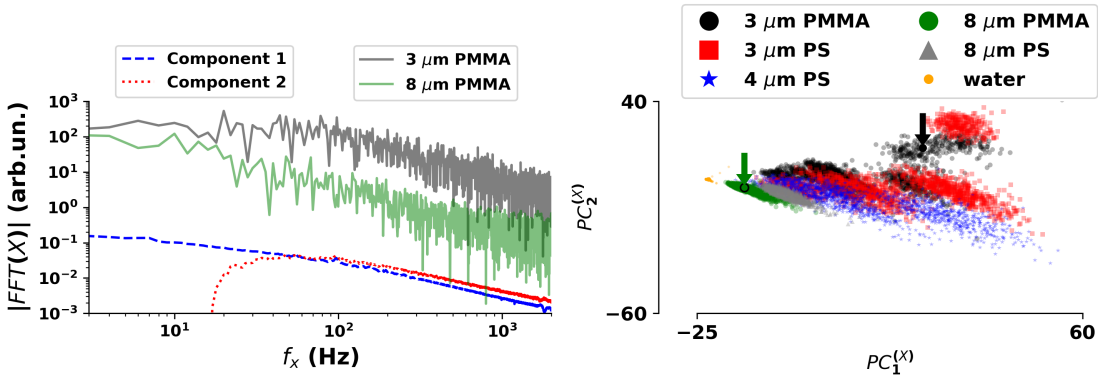

FIGURE 5.2: Results of the PCA analysis of Channel X. Left-hand side plot depicts the first two principal components obtained for the PCA analysis as well as a typical signal obtained for two distinct particles for the the X signal. Subfigure on the right-hand side displays the results of the PCA analysis as a two-dimensional plot with the first two principal components as the extracted features. The arrows represent the signals for the particles represented on the left-hand side plots.

The dimensionality reduction along with the extraction of the 6 most relevant features in the Fourier space, are essential steps to reduce the data space while keeping the dataset variation. These extracted features are based on the position fluctuations, represented in the Fourier domain, which are in principle related with the properties of the particle dynamics. Therefore, this information will be used to test the classification of particles and cells.

5.1.3 Classification algorithms implementation and evaluation procedure

The classification algorithms were implemented using the *sklearn* library, and a set of classifiers was chosen to be tested, namely Random Forests (RF), Support Vector Machines (SVM), K-Nearest Neighbors (KNN) and Neural Network (NN) classifiers (for more information related to the classification algorithms please consult the literature [89, 90]). The choice of this set with various algorithms guarantees a diverse classification strategy and to achieve the optimal performances. Resulting of the pre-processing procedure, the relevant features extracted were used to train and test each classification algorithm. In order to guarantee a trustworthy result, the accuracy was tested using a stratified x-fold cross-validation procedure. In other words, in each subset corresponding to an individual particle type, the whole set of segments is left out the train dataset, being only used as the test dataset.

In Figure 5.3, a resume of the methodology implemented for the classification task is depicted. To begin, the signals retrieved from the detector are represented (X, Y and

SUM) along with the 500 millisecond highlighted segment. Then, for each channel, the FFT algorithm is implemented, followed by the PCA analysis. Next, the most relevant components in the Fourier space are collected and used to train and test the classification algorithms.

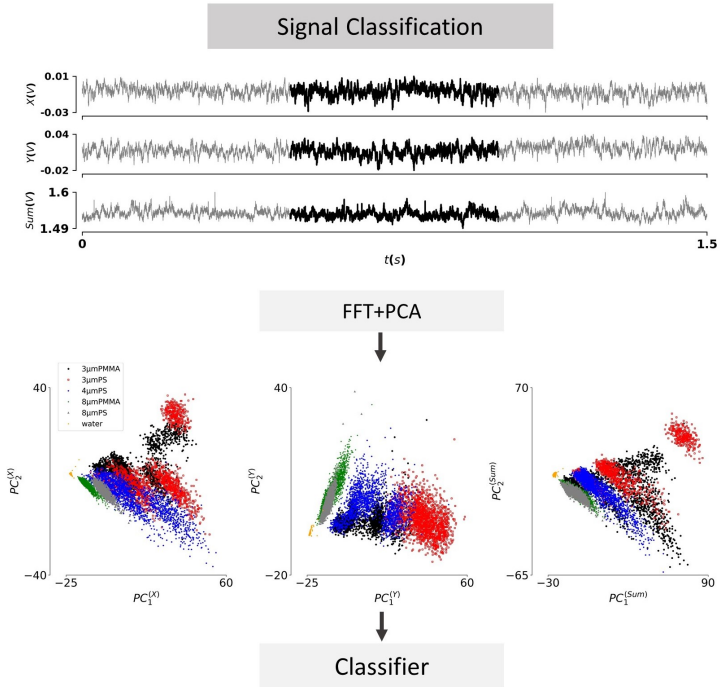

FIGURE 5.3: Schematic representation of the classification procedure, depicting the time scope of signals acquired from the quadrant photodetector (X, Y, SUM) and the PCA plots of the corresponding Fourier transforms for all the tested particles.

5.2 Results

In this section we present the results obtained for the tested particles and cells. The goal is first to validate the classifier strategy and then to test the classification capability of each algorithm in detecting the different particle classes. In particular, for each method, we present the mean, the best, and the worst performance during the 6-fold and 5-fold cross-validation procedure, as well as the confusion matrix as we shall explain shortly.

Furthermore, we present two distinct problems of classification. In the first set, we try to classify only synthetic microparticles of known dimension and composition. In the second set, the classifier tries to classify both cells and synthetic particles in which the size was not used as a discriminatory parameter. To complement the analysis, the performance of the distinct algorithms is evaluated in order to understand if a particular classifier is more suitable for one type of dataset than another.

5.2.1 Classification of micron-sized particles

The results obtained for the accuracy of the tested synthetic microparticles are depicted in Table 5.1. From a general analysis, the overall results suggest that the pre-processing procedure contains the necessary information for an effective discrimination of the particle class, validating the pre-processing procedure employed. Observing in detail the results obtained, the performance of the distinct algorithms is comparable, showing no significant variation between them. The KNN classification algorithm shows only a slightly better performance in the classification task.

TABLE 5.1: Performance results for various classification algorithms obtained for the test datasets of the cross-validation procedure for synthetic micron-sized specimens.

Method	**Accuracy - Test dataset**		
	Mean	Best	Worst
Random Forests	0.91	0.99	0.77
Support Vector Machines	0.92	0.98	0.74
K-Nearest Neighbours	0.91	0.99	0.77
Multi-layer Perceptron	0.91	0.99	0.69

In respect to the particle class discrimination, the confusion matrix for each algorithm can be computed, by accumulating the results for each cross-validation fold and normalizing them at the end. The confusion matrix is useful to interpret the results, namely to understand the classifier performance for an individual class and understand possible reasons for its underperformance. By observing the results obtained in Figure 5.4, all classes are successfully identified. Particularly, for the class that represents no trapped particles, the water class, all the classifiers were able to correctly identify it in every situation. Moreover, the large and small-sized particles were also correctly distinguished. In particular, for the $8\mu m$ size classes, the classification algorithms were able to discriminate the materials quite well, with an accuracy around 98%. However, when attempting to discriminate between the $3\mu m$ PS and $3\mu m$ PMMA class, the performance of the classifier is a bit worse, with confusion appearing with the $4\mu m$ PS class. One possible justification is the relatively small size change between the classes to be classified. Additionally, some experimental uncertainty of their actual size in the fabrication procedure or the algorithm

itself may be the cause for the incorrect identification. In both cases, further investigation is required to solve the problem and to increase the classification performance.

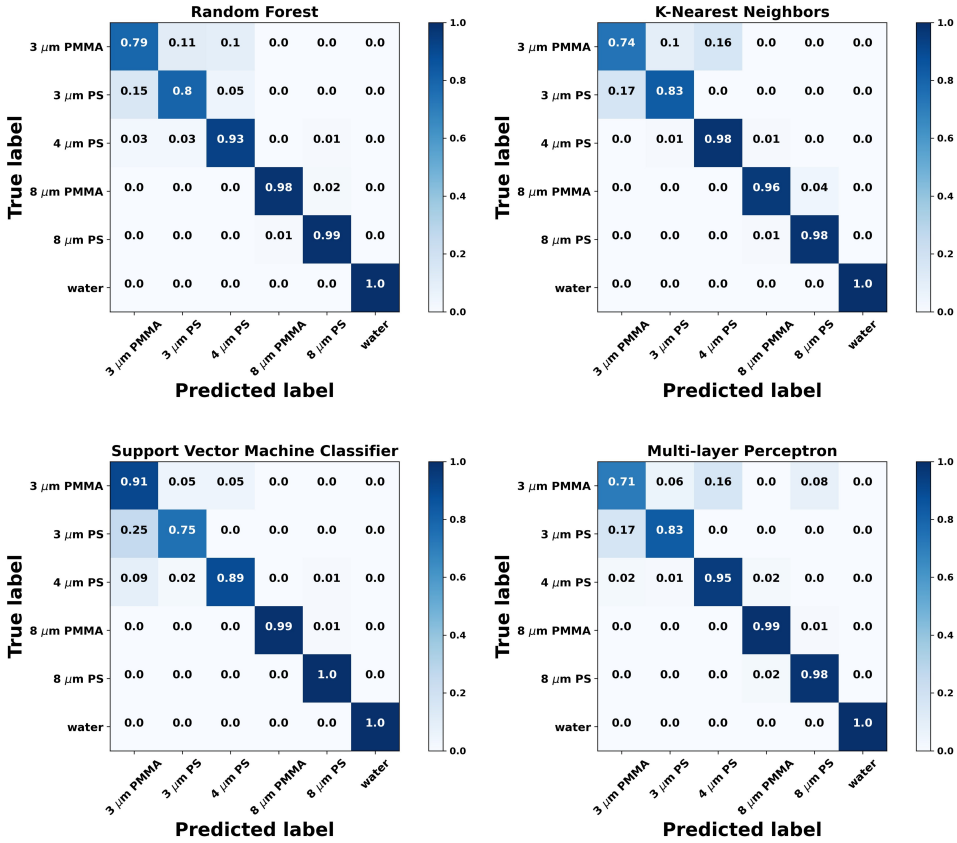

FIGURE 5.4: Confusion matrices showing the classification performance of the tested algorithms. The labels correspond to each particle type with the score corresponding to the mean accuracy obtained for the cross-validation procedure.

To understand if the the quadrant photodetector introduces any advantage over a traditional detector, the performance of using all 3-channel information was compared against that obtained using only the SUM channel. The results obtained for the accuracy of the tested synthetic microparticles, using only the SUM channel are depicted in Table 5.2. The classification performance using only the SUM channel is considerably lower, with accuracy values just above 50%. By observing the confusion matrices, depicted in Figure 5.5, the only class properly discriminated was the one that represents no trapped particles, with the algorithms being unable to correctly discriminate between the small-sized particle classes and the larger particle classes. The results obtained demonstrate the benefits of using a quadrant photodetector against a conventional photodetector for probing the forward scattered radiation which supports the merits of our approach.

TABLE 5.2: Performance results for various classification algorithms obtained for the test datasets of the cross-validation procedure for synthetic micron-sized specimens. In this case, only the *SUM* channel of the QPD is used.

Method	**Accuracy - Test dataset**		
	Mean	Best	Worst
Random Forests	0.54	0.64	0.45
Support Vector Machines	0.53	0.64	0.42
K-Nearest Neighbours	0.55	0.67	0.44
Multi-layer Perceptron	0.49	0.61	0.41

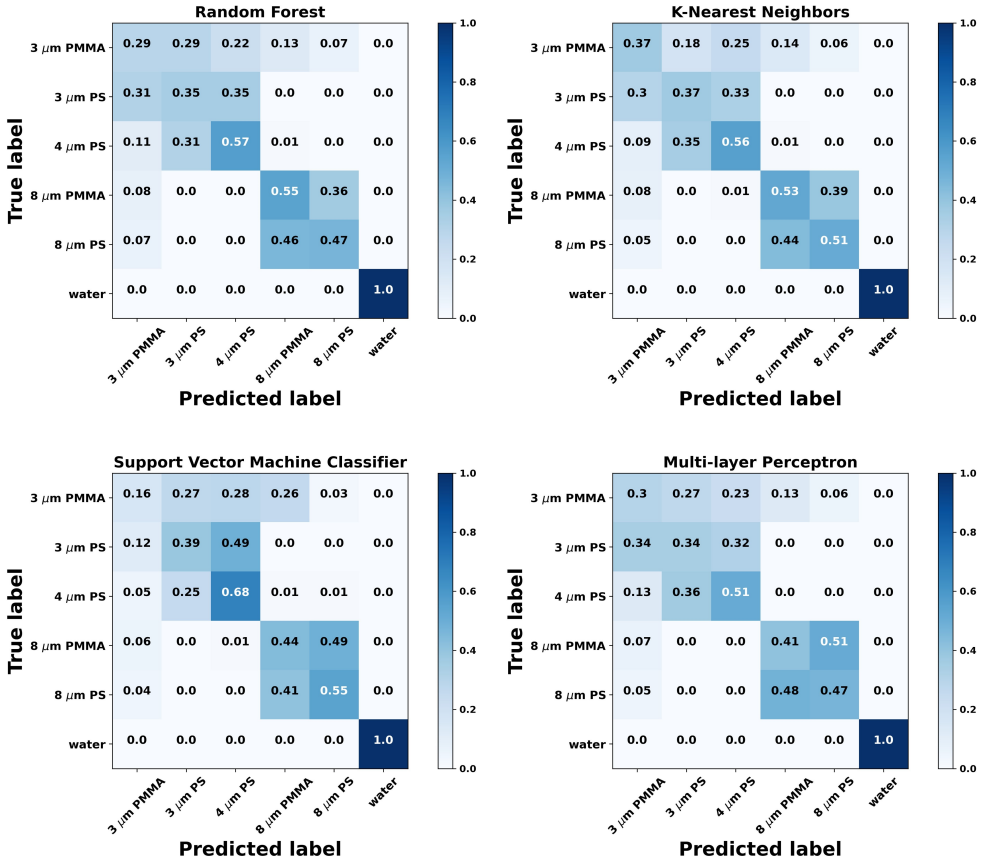

FIGURE 5.5: Confusion matrices showing the classification performance of the tested algorithms. In this case, only the *SUM* channel of the QPD is used.

5.2.2 Classification of cells

In the second set, we have tested the classification of classes with respect to the distinction of both synthetic and non synthetic specimens. The material type was considered

the only discriminatory variable, despite the fact that several sizes were employed for the same particle class.

The results obtained for the accuracy of each method are presented in Table 5.3, where the Random Forests algorithm shows a slightly better performance for this particular classification task. In comparison to the previous results, presented in Table 5.1, there is a reduction in the overall performance which is probably related with the different particle dimensions considered for the experimental measurements which disturb the class discrimination.

TABLE 5.3: Performance results for various classification algorithms obtained for the test datasets of the cross-validation procedure for synthetic and non synthetic specimens.

Method	**Accuracy - Test dataset**		
	Mean	Best	Worst
Random Forests	0.76	0.97	0.60
Support Vector Machines	0.57	0.74	0.38
K-Nearest Neighbours	0.73	0.96	0.47
Multi-layer Perceptron	0.74	0.97	0.51

In respect to each class classification, each confusion matrix is presented in Figure 5.6. The discrimination between the PS and PMMA materials was successfully achieved for all the classifiers with the exception of the SVM, whose accuracy is particularly poor. In addition, the class representative of no trapped particle was also effectively classified.

On the other hand, when attempting to discriminate the other classes, some confusion between classes appears. The low accuracy obtained for the Chllorella Vulagris and Yeast cells classification can be explained as a combination of multiple factors. Firstly, the biological specimens can have distinct composition and dimension. Therefore, size dispersion in the sample can increase the number of variables that represent that class, making the class discrimination harder. Additionally, the different composition changes the refractive index, and consequently the way that light is scattered. A second argument is related with the scattered light that can be directed out of the detector path by the specimen inner structures, and that can cause loss of information for the classification process. This is supported by the literature [91], which reports that for a cell under an optical trapping experiment, the cellular environment highly affects the light scattered. While synthetic particles do not support inner structures, the diversity and heterogeneity

of living cells can make the classification process more difficult. Finally, a last argument lays on the classification capability of the system, which can have different outcomes regarding the classes used for the discrimination. For instance, if the comparison is done with other biological samples, the results obtained can be different as the unsupervised PCA can identify other specific relevant information that can perform better for the cell classification problem.

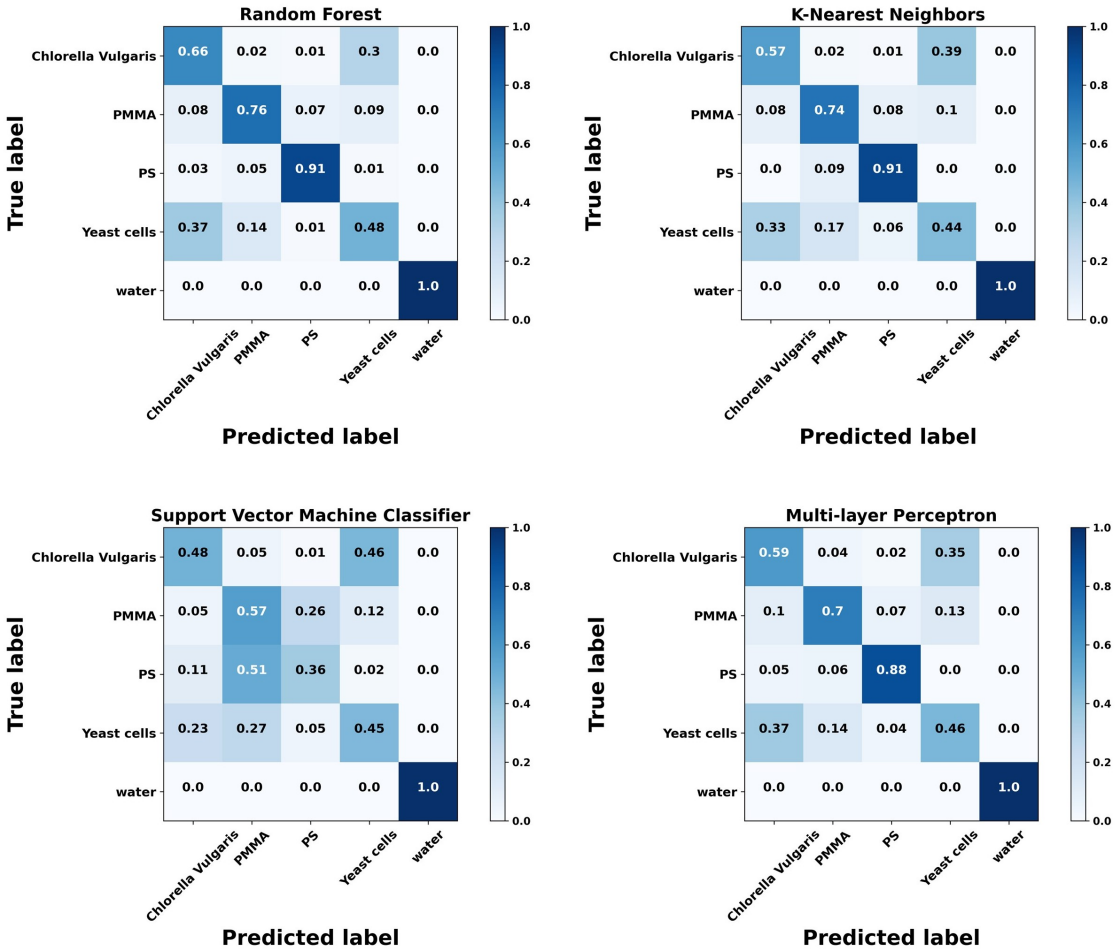

FIGURE 5.6: Confusion matrices showing the classification performance of the tested algorithms for synthetic and non synthetic specimens.

In this section, we observed that the discrimination of biological specimens is more complex due to a intrinsic variability on the size (wider size dispersion) and individual internal structure. To improve the performance, a more comprehensive training set accounting for the population variability, should be considered in future studies. Nevertheless, the discrimination between synthetic and biological specimens is already acceptable showing potential for applications where micro plastics can be separated from cells, for instance.

5.3 Benchmark against fiber optical tweezers

After proving the benefits of using a quadrant photodetector against a standard detector, we tested the classification performance of the PCA based classifier using a fiber trapping-based system.

5.3.1 Classification of micron-sized particles

The fiber trapping based setup makes use of a single mode optical fiber and a standard detector that captures the back-scattered radiation. Thus, only the most relevant components of a SUM signal can be used to train and test the algorithms, as the X and Y signals are not available. The micron-sized samples used in section 5.2.1 were first employed to test the fiber trapping system and the SUM signals retrieved using a similar methodology was submitted to data processing. This analysis enabled an insight of the classification performance of the PCA regarding the back-scattered radiation.

The results obtained for the accuracy of each method are presented in Table 5.4, with the NN algorithm showing the best performance for this classification task. In respect to each class, represented in Figure 5.7, the discrimination between the PS and PMMA materials was achieved for the smaller particles, namely for the 3 μm PS and 3 μm PMMA class with an accuracy around 60% and 80% respectively. Additionally, the class representative of no trapped particle, and the 8 μm PS class was also well distinguished. Whereas in our system the confusion between classes was verified for particles of the same size, in this case, the confusion is observed for the 8 μm PMMA class and the 4 μm PS class.

TABLE 5.4: Performance results for various classification algorithms obtained for the test datasets of the cross-validation procedure for microparticles in a fiber optical tweezers system.

Method	**Accuracy - Test dataset**		
	Mean	Best	Worst
Random Forests	0.72	0.75	0.67
Support Vector Machines	0.63	0.68	0.57
K-Nearest Neighbours	0.73	0.79	0.67
Multi-layer Perceptron	0.72	0.77	0.65

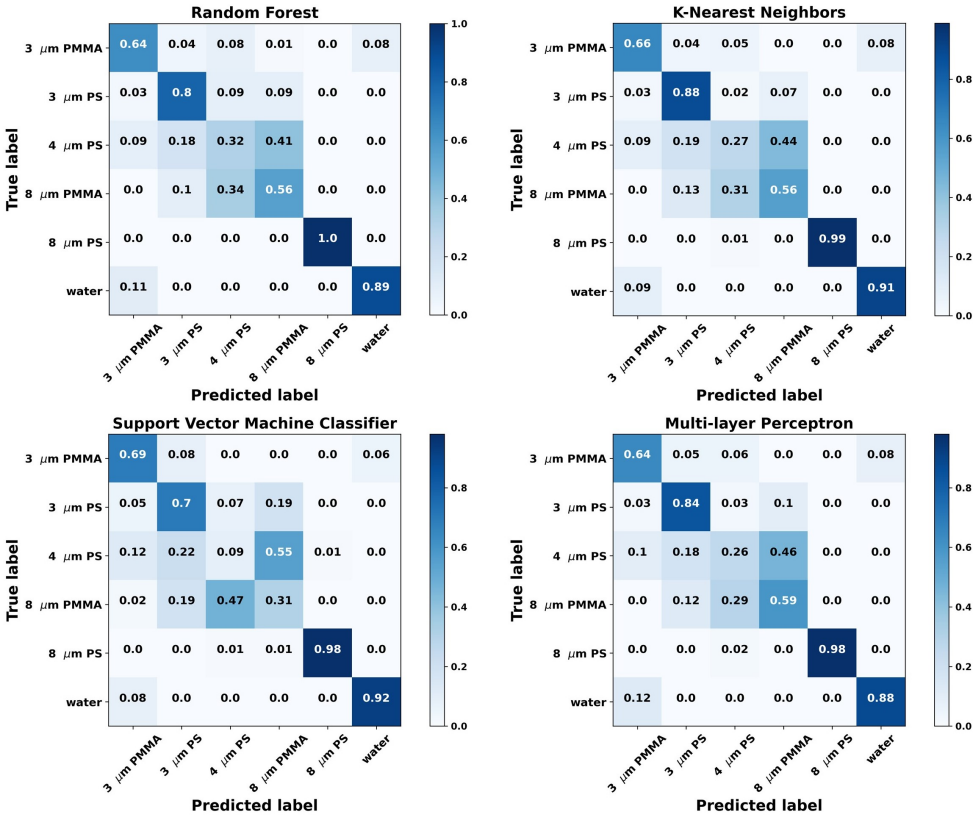

FIGURE 5.7: Confusion matrices showing the classification performance of the tested algorithms for microparticles in a fiber optical tweezers system.

By comparing the results obtained, we can infer that the performance of our PCA-based methodology is still quite good and above the one obtained using the only the *SUM* signal in the standard optical tweezers system. Thus, we could validate the fact that our classifier strategy is portable to other implementations of optical tweezers, which can pave for future studies not only with fiber optic systems but also with plasmonic ones. Nevertheless we should stress that the detection performance of the fiber tweezers system is worse than the obtained with a quadrant photodetector, which allow to infer that a conventional optical tweezers together with a position-based detection system can be an essential tool for performing tasks requiring higher accuracy rates.

5.3.2 Classification of nanoparticles

While trapping nanoparticles is not possible with a conventional optical tweezers system, the classification of these specimens using the back-scattered radiation has been reported in optical fiber trapping systems. Featuring a comparable detection capability, we decided to test the ability of our system and methodology to discriminate classes of

nanoparticles. To test that, the classification of an additional set of nanoparticles was assessed. The results obtained for the accuracy of each method are presented in Table 5.5.

TABLE 5.5: Performance results for various classification algorithms obtained for the test datasets of the cross-validation procedure for nanoparticles.

Method	**Accuracy - Test dataset**		
	Mean	Best	Worst
Random Forests	0.86	0.91	0.80
Support Vector Machines	0.86	0.90	0.80
K-Nearest Neighbours	0.86	0.91	0.81
Multi-layer Perceptron	0.85	0.89	0.80

By observing the results obtained, we see that KNN algorithm shows a better performance for this specific classification task. In respect to each class, presented in Figure 5.8, classes with the smaller sizes, namely 100 *nm* PS and 200 *nm* PS, were all successfully classified. Additionally, the class that represents no trapped particles was also successfully identified by all the classifiers. However, for the 500 *nm* size classes, that is, the 500 *nm* PS and 500 *nm* PMMA classes, the accuracy computed is lower and higher confusion of predictions appear, which might be related with the similar optical response at such small scales.

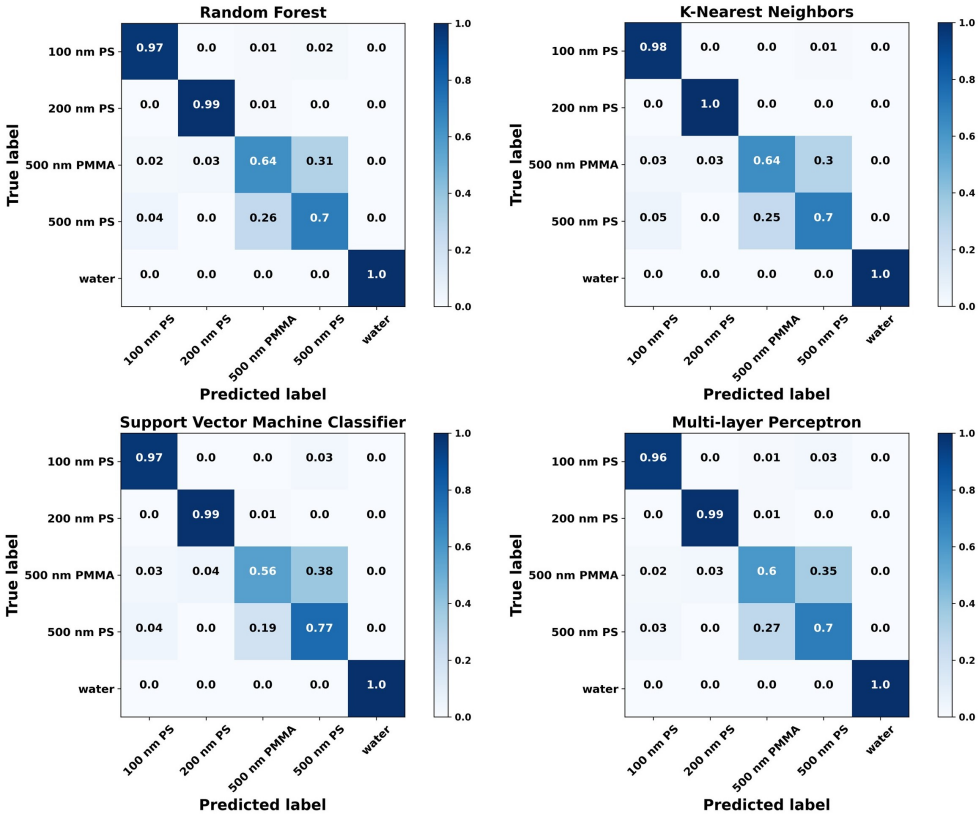

FIGURE 5.8: Confusion matrices showing the classification performance of the tested algorithms for nanoparticles.

Although there is no trapping, the algorithm still proves capable of classifying many of the classes. The most probable hypothesis is that this can be explained by a characteristic signature of each particle dynamic in the potential well, which in the Fourier space shares similar response as if the particles were effectively trapped.

Additionally, we should consider that the discrimination might be possible due to the differences in concentration (mass/vol) or particle/volume, which result in a different scattering efficiency. To disambiguate between the capability of discriminating particle type, vs particle concentration further studies and simulations shall be taken in the future for a careful and accurate proof of this conjecture, which were unable to be performed during this project due to its limited schedule. Nevertheless, the results obtained are very promising for future applications.

5.4 Concluding remarks

In this chapter, the classification of trapped particles and cells has been explored based on the data retrieved from a QPD. We presented a novel methodology based on

a pre-processing PCA procedure working in the Fourier domain for the extraction of relevant features. The pre-processed data was subsequently used to train and test some machine-learning classification algorithms with a stratified cross-validation procedure for computation of its accuracy. The results obtained suggest that this methodology can successfully discriminate both a dataset with only synthetic microparticles and another with cells and synthetic particles, in controlled experimental condition.

We have also tested the classification methodology for microparticles with an optical fiber trapping system and the classification of nano specimens in our conventional optical tweezers system. Overall the results obtained, validate the capability of standard optical tweezers system and even show some improvements over the state-of-the-art fiber-based solutions when equipped with a QPD. The proposed methodology paves for significantly faster operation rates towards real-time monitoring applications by working with smaller signal intervals, around 500 milliseconds, than those previously reported [17, 49], and leveraging on a simpler feature extraction procedure with lower computational load.

To give an example of a particular application of this methodology we can consider the characterization of a population of microalgae. Usually, to characterize a population of microalgae and study the different growth phases, the measurement of the optical density is employed. However, this approach does not ensure that the growth curve is in accordance in the real dimensions of the cells. As an alternative, by exploring a classification strategy based on optical tweezers, the discrimination of different sizes of microalgae can be attained. By using the size as a discriminatory variable, a demographic map can be obtained and consequently the control of the cell dimensions, which depend on the growing state, can be controlled in a better way.

Chapter 6

Final conclusions and future work

The purpose of this dissertation was to assemble, characterize and functionalize a conventional optical tweezers system as an analytical tool for biological purposes. In particular, by exploring the fact that trapped particles show characteristic behaviours, the final goal was to use the system for the classification of trapped specimens from their scattering signal temporal dynamics obtained with a quadrant photodetector.

In this dissertation, we described the process of assembling the standard optical tweezers system and explored its working concepts, which relies on a dynamical balance between optical-induced forces at the mesoscopic scale. The characterization of the system, the trap strength and stiffness was then accomplished. In particular we used two passive methods to compute the stiffness obtained for a set of test particles, namely the equipartition method and the power spectral density method, which presented similar results to the ones reported in the literature [92].

We then explored the setup to deploy a classification strategy for the discrimination of trapped specimens. For that, we introduced a novel pre-processing procedure based on the PCA analysis in the Fourier space for performing the relevant feature extraction. This procedure was employed for dimensionality reduction, and the features extracted were used to train and then test the performance of the classification algorithms.

For the purpose of classification, we prove the ability to classify particles and cells in an optical tweezers system. For instance, the classification of distinct micron-sized particles was successfully achieved, namely for 3 μm PMMA, 3 μm PS, 4 μm PS, 8 μm PMMA and 8 μm PS with an overall accuracy of 90%. Additionally, the discrimination of nanoparticles, with sizes ranging from 100 nm to 500 nm, presented a global accuracy around 60-70%. For the case of cells classification, namely for yeast cells and microalgae,

an overall accuracy of 50-70% was obtained, being worse when comparing to the classification of synthetic particles.

Furthermore, the results presented proved that the discrimination performance with a standard optical tweezers system, which retrieves 3-channel time signals, is significantly better in comparison to the solely channel acquisition as in a standard detector. Therefore, we believe that the use of the QPD can enhance the accuracy obtained when compared against previous approaches reported in the literature which rely on the analysis of the back-scattered radiation with a standard detector.

Finally, the method introduced leverages on a faster process for feature extraction with lower computational footprint than those previously reported in the literature. Working with signals of 500 millisecond of duration, the methodology then presents an alternative and faster classification methodology in optical trapping technologies, in comparison to the ones discussed in the state of the art.

Overall, the results validate the capability of very fast classification of microparticles and cells with a standard optical tweezers system, equipped with a QPD. We conclude that the optical tweezers presents itself as a versatile and integrated technological solution capable of performing simultaneously the discrimination and manipulation of individual particles at short time intervals. As a matter of fact, the possibility of real time performance is paramount, for biomedical applications.

6.1 Future perspectives

Due to the restrained schedule, many interesting research lines were left out of the scope of this project. Nevertheless, we shall present them in detail and discuss its possible implications.

On one hand, regarding the characterization of the system, the results we presented suggest that the trapping potential deviates from the expected symmetrical cross-section. Furthermore, the results for the trapping dynamics, suggest that the optical potential is inclined in the sample plane. Thus, further and careful studies should be undertaken in the future for a better characterization of the trapping beam. For example, the beam profile can be measured at the end of the optical fiber and before entering the system, to probe if the cross-section is indeed that of a Gaussian beam. If not, the fiber length shall be extended to allow an effective spatial filtering process, where the output would correspond to the Gaussian shape of the fiber mode profile. If it is a Gaussian, the problem

can be either in the alignment of the system or optical aberrations of the components, and therefore the knife-edge method shall be performed in other angles in the sample plane to probe the existence of a rotation angle.

On the other hand, we did not explored in detail the trapping in 3-dimensions. In particular, the stiffness constant can be computed and the optical forces characterized in the axial direction. A detailed study of the Brownian motion could also be performed to understand how distinct particles move in the trap and the validity of the assumptions made, namely the inertial regime. Also, it would be interesting to infer if this Brownian motion can be the working concept explaining why nanoparticles classification works. Moreover, the distinct concentrations (mass/vol) and particle/volume should be studied to understand how the classification performance of nanoparticles changes with these parameters.

Finally, regarding the classification methodology here introduced, it would be interesting to explore two distinct directions. First, it can be used to implement an automatic and real-time operation software to work in the laboratory. Combined with microfluidic devices, this setup would allow for fast and accurate classification tasks that can perform at the single cell level, paving the way for applications such as cell sorting and diagnosis. A second line of research is to explore the possibility of applying this same methodology in distinct contexts. Indeed, as shown in this dissertation, the proposed algorithm can both applied to conventional and fiber optical tweezers which work as a proof-of-concept for our classification strategy. Thus, it would be interesting to explore if similar results can be achieved in other configurations such as plasmonic tweezers and optical resonating devices.

Appendix A

Laser diode and Instruments specifications

A.1 Diode Laser specifications

Specifications of the Laser Diode	
Laser Reference	Lumentum s27-7602-460
Maximum operating power	460 mW
Maximum operating current	1000 mA
TEC maximum voltage	1.68 V
TEC maximum current	1.20 mA
Thermistor resistance (25ºC)	21.7-24.0 kΩ
Thermistor constant	3600-4200 K

TABLE A.1: Specifications of the most relevant parameters for the calibration of the laser diode used.

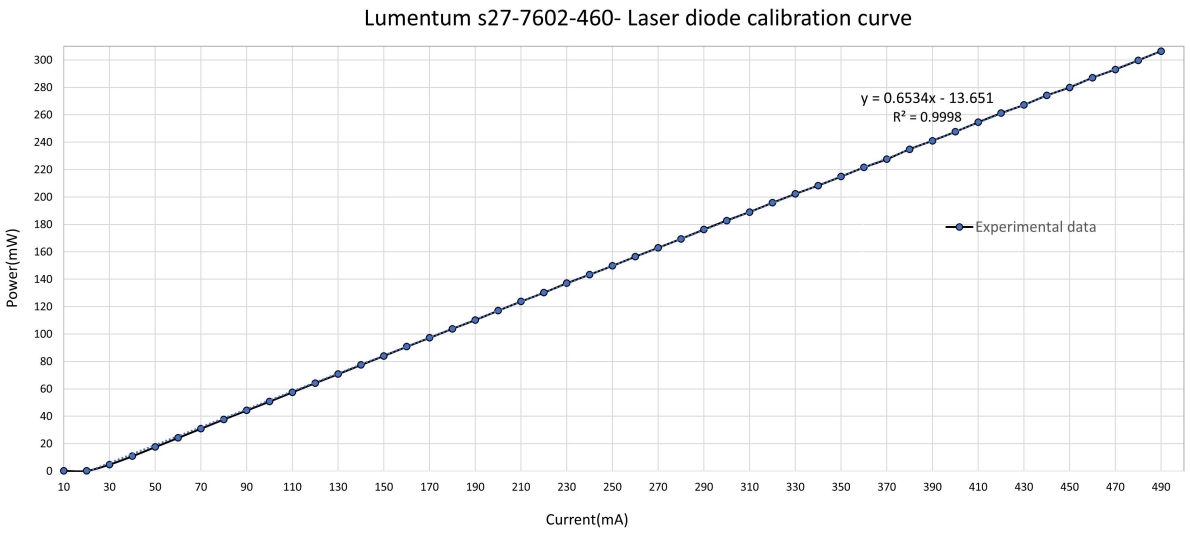

FIGURE A.1: Lumentum s27-7602-460 Laser diode characterization in terms of optical power versus the current intensity

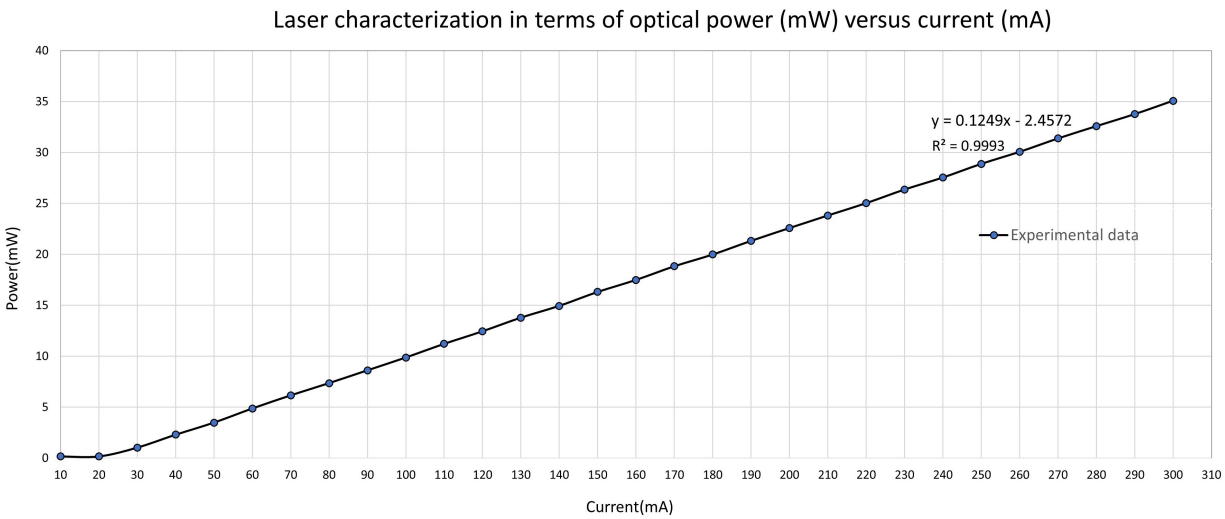

FIGURE A.2: Laser characterization in terms of optical power versus the current intensity in the sample plane.

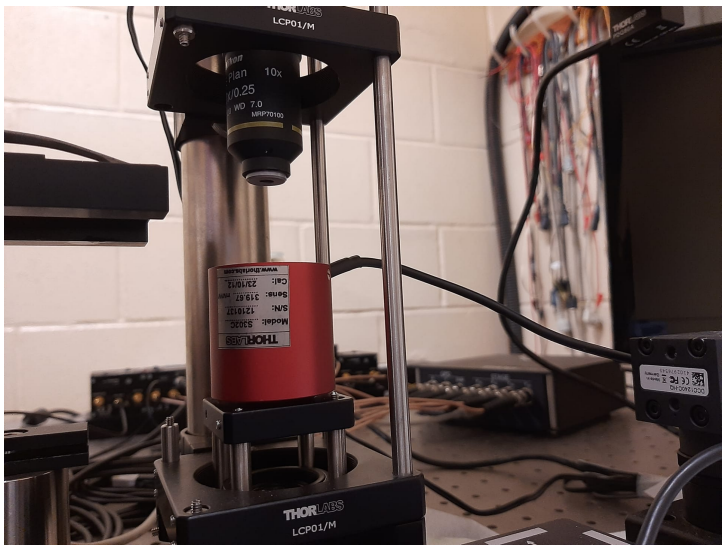

FIGURE A.3: Position where the thermal power sensor head was positioned to measure the optical power, with the power meter, just before the laser enters the objective lens.

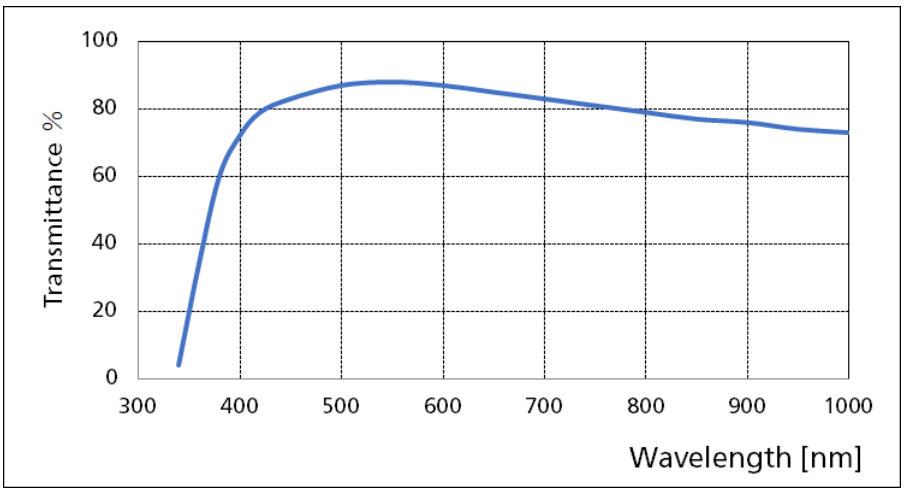

FIGURE A.4: Graph of the percentage of transmittance for a given laser beam wavelength. According to the manufacture the losses due to the microscope objective is approximately 26.25% at $976nm$ [93].

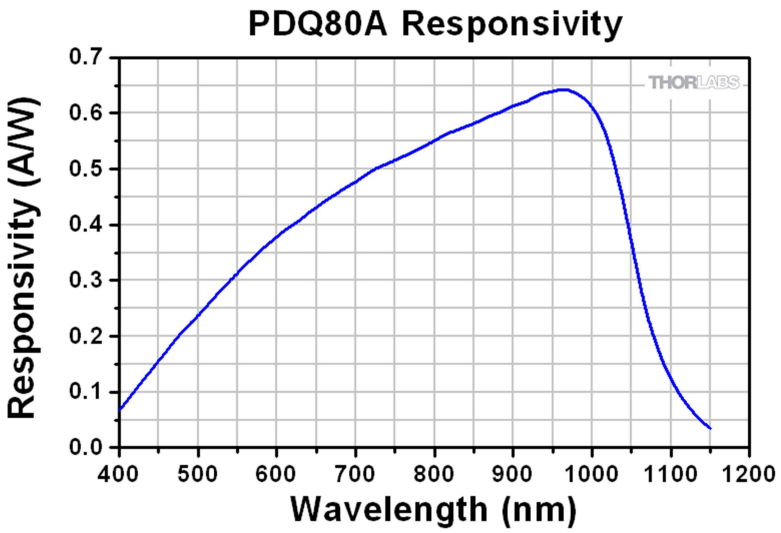

FIGURE A.5: PDQ80A quadrant photodetector responsivity curve [78].

Appendix B

Software specifications

B.1 Open loop operation mode

The open loop mode operation is usually implemented for the measurement of the position fluctuations of trapped particle over time. To implement the open loop operation mode, only precautions regarding the QPD display in APT Software must be taken into account. The position aligner must be set to Difference in X,Y Display Mode, so that the display plots the respective $XDiff$ and $YDiff$ signals. Additionally, the operating mode must be set to Monitor mode so that the difference signals are fed through the correct way. For more information please consult the respective Manual [94].

B.2 Closed loop operation mode

The OTKB and APT Software work together to implement the closed loop operation mode, for characterization of the Gaussian beam profile and for the lateral position calibration procedure. Given that, in the APT Software, the piezo controllers must be set to closed loop, so that the position over time can be measured and saved accurately, by the OTKB Software. The following steps are followed:

- APT Software
  - The piezo actuators must be in open loop operation mode.
  - In piezo settings → Drive Input Source (Open Source) → SW (Software Only).
  - Open loop → Set 35Volts to the piezo controllers.
  - Click in ENABLE button.

  - Zero the strain gauge readers (NULL count from 10 to 0).
  - Set the piezo controllers to closed loop (Analog Input Source → SMA input).
  - KPZ settings → Drive Input Source (Open Source) → VIn + wheel + SW.
  - KPZ display must be set to 46,66% of position setpoint.

- OTKB Software
  - In Data recording set 10kHz for DAQ Clock Rate
  - In Data recording set 2000 Samples per Channel
  - In Position Calibration set 10 μm to the Scan Length and set 2000 Number of Averages
  - In Position Calibration, for the knife-edge method use 300 to Number of Steps
  - In Position Calibration, for lateral position calibration use 200 to Number of Steps
  - Finally, click Run Calibration and then record the .LSdat files

Bibliography

[1] L. Novotny and B. Hecht. *Principles of nano-optics*. Cambridge University Press, 2012.

[2] A. Ashkin, J. M. Dziedzic, J. E. Bjorkholm, and S. Chu. Observation of a single-beam gradient force optical trap for dielectric particles. *Optics Letters*, 11(5):288, 1986.

[3] D. Maclssac. Nobel prize in physics awarded to arthur ashkin, gérard mourou, and donna strickland for laser physics techniques (optical tweezers and chirp pulse amplification). *The Physics Teacher*, 56(8):573–573, 2018.

[4] K. C. Neuman and S. M. Block. Optical trapping. *Review of Scientific Instruments*, 75(9):2787–2809, 2004.

[5] R. Zhu, T. Avsievich, A. Popov, and I. Meglinski. Optical tweezers in studies of red blood cells. *Cells*, 9(3):545, 2020.

[6] J. S. Paiva. *Intelligent Lab on Fiber tools for sensing single-cells and extracellular nanovesicles*. PhD thesis, Faculdade de Ciências da Universidade do Porto, 2019.

[7] A. Ashkin. Acceleration and trapping of particles by radiation pressure. *Physical Review Letters*, 24(4):156–159, 1970.

[8] A. Ashkin. Forces of a single-beam gradient laser trap on a dielectric sphere in the ray optics regime. *Biophysical Journal*, 61(2):569–582, 1992.

[9] S. Chu, J. E. Bjorkholm, A. Ashkin, and A. Cable. Experimental observation of optically trapped atoms. *Physical Review Letters*, 57(3):314–317, 1986.

[10] P. H. Jones, O. M. Maragò, and G. Volpe. *Optical tweezers: principles and applications*. Cambridge University Press, 2015.

[11] A. Ashkin and J. Dziedzic. Optical trapping and manipulation of viruses and bacteria. *Science*, 235(4795):1517–1520, 1987.

[12] A. Ashkin, J. M. Dziedzic, and T. Yamane. Optical trapping and manipulation of single cells using infrared laser beams. *Nature*, 330(6150):769–771, 1987.

[13] M. W. Berns, W. H. Wright, B. J. Tromberg, G. A. Profeta, J. J. Andrews, and R. J. Walter. Use of a laser-induced optical force trap to study chromosome movement on the mitotic spindle. *Proceedings of the National Academy of Sciences*, 86(12):4539–4543, 1989.

[14] I. A. Favre-Bulle, A. B. Stilgoe, E. K. Scott, and H. Rubinsztein-Dunlop. Optical trapping in vivo: theory, practice, and applications. *Nanophotonics*, 8(6):1023–1040, 2019.

[15] K. Svoboda and S. M. Block. Biological applications of optical forces. *Annual Review of Biophysics and Biomolecular Structure*, 23(1):247–285, 1994.

[16] D. G. Grier. A revolution in optical manipulation. *Nature*, 424(6950):810–816, 2003.

[17] J. S. Paiva, P. A. S. Jorge, R. S. R. Ribeiro, M. Balmaña, D. Campos, S. Mereiter, C. Jin, N. G. Karlsson, P. Sampaio, C. A. Reis, and et al. ilof: An intelligent lab on fiber approach for human cancer single-cell type identification. *Scientific Reports*, 10(1), 2020.

[18] P. Polimeno, Al. Magazzù, M. A. Iatì, F. Patti, R. Saija, C. Degli Esposti Boschi, M. G. Donato, P. G. Gucciardi, P. H. Jones, G. Volpe, and O. M. Maragò. Optical tweezers and their applications. *Journal of Quantitative Spectroscopy and Radiative Transfer*, 218:131–150, 2018.

[19] J. S. Paiva, P. A. S. Jorge, R. S. R. Ribeiro, P. Sampaio, C. C. Rosa, and J. P. S. Cunha. Optical fiber-based sensing method for nanoparticle detection through supervised back-scattering analysis: a potential contributor for biomedicine. *International Journal of Nanomedicine*, Volume 14:2349–2369, 2019.

[20] K. M. Candelario and D. A. Steindler. The role of extracellular vesicles in the progression of neurodegenerative disease and cancer. *Trends in Molecular Medicine*, 20(7):368–374, 2014.

[21] I. C. D. Lenton, E. K. Scott, H. Rubinsztein-Dunlop, and I. A. Favre-Bulle. Optical tweezers exploring neuroscience. *Frontiers in Bioengineering and Biotechnology*, 8, 2020.

[22] I. Prada, M. Gabrielli, E. Turola, A. Iorio, G. D'Arrigo, R. Parolisi, M. De Luca, M. Pacifici, M. Bastoni, M. Lombardi, and et al. Glia-to-neuron transfer of mirnas via extracellular vesicles: a new mechanism underlying inflammation-induced synaptic alterations. *Acta Neuropathologica*, 135(4):529–550, 2018.

[23] M. J. Lang, C. L. Asbury, J. W. Shaevitz, and S. M. Block. An automated two-dimensional optical force clamp for single molecule studies. *Biophysical Journal*, 83(1):491–501, 2002.

[24] F. Gittes and C. F. Schmidt. Interference model for back-focal-plane displacement detection in optical tweezers. *Optics Letters*, 23(1):7, 1998.

[25] A. Rohrbach and E. H. K. Stelzer. Three-dimensional position detection of optically trapped dielectric particles. *Journal of Applied Physics*, 91(8):5474–5488, 2002.

[26] H. Liu, H. Hu, M. Tie, W. Zhang, and Y. Shen. Back-focal-plane interferometry for 3d position tracking in optical tweezers. pages 1–4, 05 2012.

[27] M. W. Allersma, F. Gittes, M. J. Decastro, R. J. Stewart, and C. F. Schmidt. Two-dimensional tracking of ncd motility by back focal plane interferometry. *Biophysical Journal*, 74(2):1074–1085, 1998.

[28] A. Ashkin, K. Schütze, J. M. Dziedzic, U. Euteneuer, and M. Schliwa. Force generation of organelle transport measured in vivo by an infrared laser trap. *Nature*, 348(6299):346–348, 1990.

[29] M. Sarshar, W. T. Wong, and B. Anvari. Comparative study of methods to calibrate the stiffness of a single-beam gradient-force optical tweezers over various laser trapping powers. *Journal of Biomedical Optics*, 19(11):115001, 2014.

[30] K. Berg-Sørensen and H. Flyvbjerg. Power spectrum analysis for optical tweezers. *Review of Scientific Instruments*, 75(3):594–612, 2004.

[31] E.-L. Florin, A. Pralle, E. H.K. Stelzer, and J. K.H. Hörber. Photonic force microscope calibration by thermal noise analysis. *Applied Physics A: Materials Science & Processing*, 66(7), 1998.

[32] M. Ribezzi-Crivellari, J. M. Huguet, and F. Ritort. Counter-propagating dual-trap optical tweezers based on linear momentum conservation. *Review of Scientific Instruments*, 84(4):043104, 2013.

[33] W. Grange, S. Husale, H.-J. Güntherodt, and M. Hegner. Optical tweezers system measuring the change in light momentum flux. *Review of Scientific Instruments*, 73(6):2308–2316, 2002.

[34] J. Gieseler, J. R. Gomez-Solano, A. Magazzù, I. P. Castillo, L. P. García, M. Gironella-Torrent, X. Viader-Godoy, F. Ritort, G. Pesce, A. V. Arzola, K. Volke-Sepúlveda, and G. Volpe. Optical tweezers — from calibration to applications: a tutorial. *Adv. Opt. Photon.*, 13(1):74–241, Mar 2021.

[35] S. Yadav, R. Vadivelu, M. Ahmed, M. Barton, and N.-T. Nguyen. Stretching cells – an approach for early cancer diagnosis. *Experimental Cell Research*, 378(2):191–197, 2019.

[36] D. Wang and S. Bodovitz. Single cell analysis: the new frontier in 'omics'. *Trends in Biotechnology*, 28(6):281–290, 2010.

[37] M. Pradhan, S. Pathak, D. Mathur, and U. Ladiwala. Optically trapping tumor cells to assess differentiation and prognosis of cancers. *Biomedical Optics Express*, 7(3):943, 2016.

[38] J. P. M. de Sá. *Pattern recognition: concepts, methods, and applications*. Springer, 2001.

[39] X. Wang, S. Chen, M. Kong, Z. Wang, K. D. Costa, R. A. Li, and D. Sun. Enhanced cell sorting and manipulation with combined optical tweezer and microfluidic chip technologies. *Lab on a Chip*, 11(21):3656–3662, 2011.

[40] C. Ti, M.-T. Ho-Thanh, Q. Wen, and Y. Liu. Objective-lens-free fiber-based position detection with nanometer resolution in a fiber optical trapping system. *Scientific reports*, 7(1):1–10, 2017.

[41] L. Xie, Q. Liu, C. Shao, and X. Su. Differentiation of normal and leukemic cells by 2d light scattering label-free static cytometry. *Optics Express*, 24(19):21700, 2016.

[42] B. Redding, M. Schwab, and Y.-L. Pan. Raman spectroscopy of optically trapped single biological micro-particles. *Sensors*, 15(8):19021–19046, 2015.

[43] C. N. Lafratta. Optical tweezers for medical diagnostics. *Analytical and Bioanalytical Chemistry*, 405(17):5671–5677, 2013.

[44] B. Redding, M. Schwab, and Y.-L. Pan. Raman spectroscopy of optically trapped single biological micro-particles. *Sensors*, 15(8):19021–19046, 2015.

[45] M. Grimm, T. Franosch, and S. Jeney. High-resolution detection of brownian motion for quantitative optical tweezers experiments. *Physical Review E*, 86(2):021912, 2012.

[46] K. Berg-Sørensen and H. Flyvbjerg. Power spectrum analysis for optical tweezers. *Review of Scientific Instruments*, 75(3):594–612, 2004.

[47] I. C. D. Lenton, G. Volpe, A. B. Stilgoe, T. A. Nieminen, and H. Rubinsztein-Dunlop. Machine learning reveals complex behaviours in optically trapped particles. *Machine Learning: Science and Technology*, 1(4):045009, 2020.

[48] R. S. R. Ribeiro, O. Soppera, A. G. Oliva, A. Guerreiro, and P. A. S. Jorge. New trends on optical fiber tweezers. *Journal of Lightwave Technology*, 33(16):3394–3405, 2015.

[49] J. S. Paiva, P. A. S. Jorge, C. C. Rosa, and J. P. S. Cunha. Optical fiber tips for biological applications: From light confinement, biosensing to bioparticles manipulation. *Biochimica et Biophysica Acta (BBA) - General Subjects*, 1862(5):1209–1246, 2018.

[50] Y. Pang and R. Gordon. Optical trapping of 12 nm dielectric spheres using double-nanoholes in a gold film. *Nano Letters*, 11(9):3763–3767, 2011.

[51] Y. Pang and R. Gordon. Optical trapping of a single protein. *Nano Letters*, 12(1):402–406, 2011.

[52] R. Gordon. Biosensing with nanoaperture optical tweezers. *Optics & Laser Technology*, 109:328–335, 2019.

[53] R. S. R. Ribeiro. *Optical fiber tools for single cell trapping and maipulation*. PhD thesis, Faculdade de Ciências da Universidade do Porto, 2017.

[54] R. S. R. Ribeiro, P. Dahal, A. Guerreiro, P. A. S. Jorge, and J. Viegas. Fabrication of fresnel plates on optical fibres by fib milling for optical trapping, manipulation and detection of single cells. *Scientific Reports*, 7(1), 2017.

[55] I. Leite, S. Turtaev, X. Jiang, M. Siler, A. Cuschieri, P. Russell, and T. Čižmár. Three-dimensional holographic optical manipulation through a high-numerical-aperture soft-glass multimode fibre. *Nature Photonics*, 12, 01 2018.

[56] A. Ashkin. History of optical trapping and manipulation of small-neutral particle, atoms, and molecules. *IEEE Journal of Selected Topics in Quantum Electronics*, 6(6):841–856, 2000.

[57] O. M. Maragò, P. H. Jones, P. G. Gucciardi, G. Volpe, and A. C. Ferrari. Optical trapping and manipulation of nanostructures. *Nature Nanotechnology*, 8(11):807–819, 2013.

[58] D. G. Kotsifaki and S. N. Chormaic. Plasmonic optical tweezers based on nanostructures: fundamentals, advances and prospects. *Nanophotonics*, 8(7):1227–1245, 2019.

[59] J.-S. Huang and Y.-T. Yang. Origin and future of plasmonic optical tweezers. *Nanomaterials*, 5(2):1048–1065, 2015.

[60] L. Novotny, R. X. Bian, and X. S. Xie. Theory of nanometric optical tweezers. *Physical Review Letters*, 79(4):645–648, 1997.

[61] K. Okamoto and S. Kawata. Radiation force exerted on subwavelength particles near a nanoaperture. *Physical Review Letters*, 83(22):4534–4537, 1999.

[62] M. L. Juan, R. Gordon, Y. Pang, F. Eftekhari, and R. Quidant. Self-induced back-action optical trapping of dielectric nanoparticles. *Nature Physics*, 5(12):915–919, 2009.

[63] L. Neumeier, R. Quidant, and D. E. Chang. Self-induced back-action optical trapping in nanophotonic systems. *New Journal of Physics*, 17(12):123008, 2015.

[64] M. L. Juan, M. Righini, and R. Quidant. Plasmon nano-optical tweezers. *Nature Photonics*, 5(6):349–356, 2011.

[65] F. Vollmer and S. Arnold. Whispering-gallery-mode biosensing: label-free detection down to single molecules. *Nature Methods*, 5(7):591–596, 2008.

[66] J. Su, A. FG. Goldberg, and B. M. Stoltz. Label-free detection of single nanoparticles and biological molecules using microtoroid optical resonators. *Light: Science & Applications*, 5(1), 2016.

[67] F. Vollmer, S. Arnold, and D. Keng. Single virus detection from the reactive shift of a whispering-gallery mode. *Proceedings of the National Academy of Sciences*, 105(52):20701–20704, 2008.

[68] S. Arnold, D. Keng, S. I. Shopova, S. Holler, W. Zurawsky, and F. Vollmer. Whispering gallery mode carousel – a photonic mechanism for enhanced nanoparticle detection in biosensing. *Optics Express*, 17(8):6230, 2009.

[69] P. Vaiano, B. Carotenuto, M. Pisco, A. Ricciardi, G. Quero, M. Consales, A. Crescitelli, E. Esposito, and A. Cusano. Lab on fiber technology for biological sensing applications. *Laser & Photonics Reviews*, 10(6):922–961, 2016.

[70] L. H. Øgendal. Light scattering demystified: Theory and practice, 9 2017.

[71] R. Xu. *Particle Characterization: Light Scattering Methods*, volume 13. Springer Netherlands, 1 edition, 2002.

[72] K. Tsia. Understanding biophotonics : Fundamentals, advances, and applications. 2015.

[73] E. Hecht. *Optics*. Pearson, 2016.

[74] A. Bérut. *Fluctuations and Interactions of Brownian particles in multiple Optical Traps*. PhD thesis, 07 2015.

[75] G. Volpe and G. Volpe. Simulation of a brownian particle in an optical trap. *American Journal of Physics*, 81(3):224–230, 2013.

[76] MIT Department of Physics . Optical Trapping, 2017.

[77] D. Appleyard, K. Vandermeulen, H. Lee, and M. Lang. Optical trapping for undergraduates. *American Journal of Physics*, 75:5–14, 01 2007.

[78] Thorlabs. Quadrant position photodiode detectors.

[79] A. A. M. Bui, A. V. Kashchuk, M. A. Balanant, T. A. Nieminen, H. Rubinsztein-Dunlop, and A. B. Stilgoe. Calibration of force detection for arbitrarily shaped particles in optical tweezers, Jul 2018.

[80] A. Vera-Marquina, A. Diaz-sanchez, J. Rocha-Pérez, D. Berman-Mendoza, and I. Padilla. Quadrant photodiode for electronic processing. *Proc SPIE*, 7419, 08 2009.

[81] T. Khaled. Design and simulation of an intelligent laser tracking system. 2016.

[82] D. Marett. Conspiracy of light. http://www.conspiracyoflight.com/Quadrant/Quadrant.html, 2021. Accessed on 05.07.2021.

[83] N. Sultanova, S. Kasarova, and I. Nikolov. Dispersion properties of optical polymers. *Acta Physica Polonica A*, 116(4):585–587, 2009.

[84] P. M. Rowe, M. Fergoda, and S. Neshyba. Temperature-dependent optical properties of liquid water from 240 to 298 k. *Journal of Geophysical Research: Atmospheres*, 125(17), 2020.

[85] M. A. De Araújo, R. Silva, E. De Lima, D. P. Pereira, and P. C. De Oliveira. Measurement of gaussian laser beam radius using the knife-edge technique: improvement on data analysis. *Applied Optics*, 48(2):393, 2009.

[86] M. F. M. Yusof, M. S. M. Yeng, and S. K. Ayop. Axial calibration of qpd signal based on stuck bead method for optical trapping applications. *International Journal of Engineering & Technology*, 7(4.30):371, 2018.

[87] P. Yale, J.-M. Konin, M. Kouacou, and J. Zoueu. New detector sensitivity calibration and the calculation of the interaction force between particles using an optical tweezer. *Micromachines*, 9(9):425, 2018.

[88] M. Ringnér. What is principal component analysis? *Nature Biotechnology*, 26(3):303–304, 2008.

[89] S. Kotsiantis, I. Zaharakis, and P. Pintelas. Supervised machine learning: A review of classification techniques. *Informatica*, 31, 2007.

[90] S. Shalev-Shwartz and S. Ben-David. *Understanding machine learning: from theory to algorithms*. Cambridge University Press, 2014.

[91] Y.-J. Su and L. Hsu. Comparison of backward-scattered detection and forward-scattered detection for measuring optical force in optical tweezers. *Optical Trapping and Optical Micromanipulation VII*, 2010.

[92] C. Riesenberg, C. A. Iriarte-Valdez, A. Becker, M. Dienerowitz, A. Heisterkamp, A. Ngezahayo, and M. L. Torres-Mapa. Probing ligand-receptor interaction in living cells using force measurements with optical tweezers. *Frontiers in Bioengineering and Biotechnology*, 8, 2020.

[93] Cfi e plan achromat series. https://www.microscope.healthcare.nikon.com/products/optics/cfi-e-plan-achromat-series, 2021. Accessed on 10.08.2021.

[94] Thorlabs. KPA101 Beam Position Aligner, 2017.